The Astrophysical Journal, 950:33 (22pp), 2023 June 10 https://doi.org/10.3847/1538-4357/acca7c
© 2023. The Author(s). Published by the American Astronomical Society.
OPEN ACCESS

A Comparison of Outflow Properties in AGN Dwarfs versus Star-forming Dwarfs

Archana Aravindan[1], Weizhe Liu[2], Gabriela Canalizo[1], Sylvain Veilleux[3,4], Thomas Bohn[5], Remington O. Sexton[6,7], David S. N. Rupke[8], and Vivian U[9]
[1] Department of Physics and Astronomy, University of California, Riverside, 900 University Ave., Riverside CA 92521, USA; aarav005@ucr.edu
[2] Steward Observatory, University of Arizona, 933 N. Cherry Ave., Tucson, AZ 85719, USA
[3] Department of Astronomy, University of Maryland, College Park, MD 20742, USA
[4] Joint Space-Science Institute, University of Maryland, College Park, MD 20742, USA
[5] Hiroshima Astrophysical Science Center, Hiroshima University, 1-3-1 Kagamiyama, Higashi-Hiroshima, Hiroshima 739-8526, Japan
[6] George Mason University, Department of Physics and Astronomy, MS3F3, 4400 University Dr., Fairfax, VA 22030, USA
[7] U.S. Naval Observatory, 3450 Massachusetts Ave. NW, Washington, DC 20392-5420, USA
[8] Department of Physics, Rhodes College, Memphis, TN 38112, USA
[9] Department of Physics and Astronomy, 4129 Frederick Reines Hall, University of California, Irvine, CA 92697, USA
Received 2023 January 23; revised 2023 March 20; accepted 2023 April 3; published 2023 June 8

Abstract

Feedback likely plays a crucial role in resolving discrepancies between observations and theoretical predictions of dwarf galaxy properties. Stellar feedback was once believed to be sufficient to explain these discrepancies, but it has thus far failed to fully reconcile theory and observations. The recent discovery of energetic galaxy-wide outflows in dwarf galaxies hosting active galactic nuclei (AGNs) suggests that AGN feedback may have a larger role in the evolution of dwarf galaxies than previously suspected. In order to assess the relative importance of stellar versus AGN feedback in these galaxies, we perform a detailed Keck/KCWI optical integral field spectroscopic study of a sample of low-redshift star-forming (SF) dwarf galaxies that show outflows in ionized gas in their Sloan Digital Sky Survey spectra. We characterize the outflows and compare them to observations of AGN-driven outflows in dwarfs. We find that SF dwarfs have outflow components that have comparable widths (W_{80}) to those of outflows in AGN dwarfs, but are much less blueshifted, indicating that SF dwarfs have significantly slower outflows than their AGN counterparts. Outflows in SF dwarfs are spatially resolved and significantly more extended than those in AGN dwarfs. The mass-loss, momentum, and energy rates of star-formation-driven outflows are much lower than those of AGN-driven outflows. Our results indicate that AGN feedback in the form of gas outflows may play an important role in dwarf galaxies and should be considered along with SF feedback in models of dwarf galaxy evolution.

Unified Astronomy Thesaurus concepts: Dwarf galaxies (416); Extragalactic astronomy (506); Stellar winds (1636); Active galactic nuclei (16); Galaxy evolution (594); Star formation (1569)

1. Introduction

Dwarf galaxies are some of the most abundant objects in the universe with stellar masses $< \sim 10^{10}\ M_{\odot}$. They form an important part of cosmological simulations used to study the early universe. However, observations of dwarf galaxies have posed several challenges, particularly because some of these observations are at odds with ΛCDM models. Examples of these discrepancies include the core–cusp problem (Dubinski & Carlberg 1991; Navarro et al. 1996), the missing satellites problem (Klypin et al. 1999; Moore et al. 1999), and the too-big-to-fail problem (Boylan-Kolchin et al. 2011), among several others (for a comprehensive review of the challenges for cosmological models of dwarf galaxies see Sales et al. 2022). The most widely accepted solution to all these issues has been to incorporate the effects of feedback in the models.

Stellar feedback, believed to be the dominant source of feedback in dwarf galaxies (Larson 1974; Veilleux et al. 2005; Martín-Navarro & Mezcua 2018), usually originates from outflows and fast winds from star-forming (SF) regions and supernova (SN) explosions. There have been contrasting results regarding the role of stellar feedback in resolving the discrepancies between predictions and models. For example, Mashchenko et al. (2008) indicated that random bulk motions of gas driven by SN explosions would result in the flattening of the central dark matter cusp while Ogiya & Mori (2011) argued that the mass loss driven by stellar feedback might not be an effective mechanism to flatten the central cusp. Sawala et al. (2016) showed that SN feedback is sufficient to explain both the missing satellites problem and the too-big-to-fail problem, while Boylan-Kolchin et al. (2012) and Garrison-Kimmel et al. (2013) modeled the effects of SN feedback using high-resolution numerical simulations and concluded that SN feedback alone is unlikely to explain the too-big-to-fail problem in Milky Way subhaloes.

Such contrasting results could possibly indicate that stellar feedback alone may not be sufficient to explain the discrepancies between models and observations. The recent increase in the number of active black holes (i.e., active galactic nuclei or AGNs) detected in dwarf galaxies (e.g., Greene & Ho 2007; Reines et al. 2013; Moran et al. 2014; Mezcua & Domínguez Sánchez 2020; Molina et al. 2021) has raised the possibility that AGN feedback could play a prominent role in fixing the unresolved discrepancies. The effect of AGN-powered feedback is well known in massive galaxies (Rupke & Veilleux 2013a, 2013b; Harrison et al.

Original content from this work may be used under the terms of the Creative Commons Attribution 4.0 licence. Any further distribution of this work must maintain attribution to the author(s) and the title of the work, journal citation and DOI.

2014; Veilleux et al. 2014; Rupke & Veilleux 2015; Lau et al. 2018; Ramos Almeida et al. 2019). However, most of the current cosmological models for dwarf galaxies do not incorporate AGN feedback, either due to limitations in resolution or because of assumptions that AGN-powered feedback does not contribute significantly to the evolution of dwarf galaxies (Sijacki et al. 2015).

There have been increasing arguments in favor of incorporating AGN feedback in dwarf galaxies' models. Dashyan et al. (2018) found that AGN feedback is more effective than SN feedback in dwarf galaxies by comparing analytically modeled properties of outflows from both sources. High-resolution cosmological zoom-in simulations of dwarf galaxies also show that AGN feedback is more relevant than stellar feedback in dwarf galaxies (Koudmani et al. 2021, 2022).

Observationally, AGN feedback in the form of AGN-driven outflows has been discovered in many dwarf galaxies. Penny et al. (2018) found evidence of an ionized gas component that is kinematically offset from the stellar component, possibly indicating outflowing gas. Manzano-King et al. (2019) found evidence of strong and powerful outflows in dwarf galaxies that contain AGNs. Following that, Liu et al. (2020, hereafter L20) did a comprehensive study of dwarf galaxies with AGNs from the Manzano-King et al. (2019) sample using integral field spectroscopy (IFS) from Keck/KCWI. They found that warm ionized outflows were detected in six of the eight targets, with broad, blueshifted fast outflows ($v_{50} \sim -240$ km s^{-1} and $W_{80} \sim -1200$ km s^{-1}). They also calculated the energetics of the outflows and determined that a sizable ionized gas mass ($\sim 10^{-3}$–10^{-1} $M_\odot$ yr^{-1}) was present in the outflows. In addition, the outflows had significant kinetic energy outflow rates ($\sim 10^{37}$–10^{40} erg s^{-1}). These significant values indicate that AGNs can play an important role in clearing out gas and material from dwarf galaxies or otherwise in suppressing their star formation.

In order to make robust claims about the relevance of AGN feedback in dwarf galaxies, it is important to directly compare these values to the energetics found in outflows powered by stellar processes. The kinematics of ionized gas in nearby starburst and irregular dwarf galaxies have been probed using H I, Hα, and Na D (Schwartz & Martin 2004; van Eymeren et al. 2009, 2010). Those studies found outflows with velocities around 20–60 km s^{-1}, which are too slow for the gas in them to escape the gravitational potential of their host galaxies and are therefore less likely to serve as negative feedback in these dwarf galaxies. Marasco et al. (2023) studied the kinematics of ionized gas in a sample of 19 nearby starburst dwarf galaxies. Based on the modeling of the Hα velocity profiles from MUSE data, they found that the velocity fields in these starburst galaxies have speeds of a few tens of kilometers per second, which is much less than the speeds reached by AGN-powered outflows found by L20. They also found that the mass outflow rates caused by winds in the galaxies are around 10^{-4}–10^{-1} $M_\odot$ yr^{-1}.

In this paper, we attempt to provide a direct comparison between AGN-driven and stellar-driven outflows in dwarf galaxies. We use a similar analysis to that of L20 on a control sample of 10 SF dwarf galaxies using IFS. The paper is organized as follows: In Section 2, we describe the sample selection, present details of the targets, and describe the observations and data reduction. In Section 3, we list the details of the fitting of the emission lines. In Section 4, we present the main characteristics of the outflows that were detected in the sample and the calculations of the energetics. We compare our results to those of L20 wherever possible and present our conclusions and their implications in Section 5, and in Section 6, we summarize our results. More details about the individual targets can be found in the Appendix. Throughout the paper we assume the same ΛCDM cosmology of L20, with $H_0 = 69.3$ km s^{-1} Mpc^{-1}, $\Omega_m = 0.287$, and $\Omega_\Lambda = 0.713$ (Hinshaw et al. 2013).

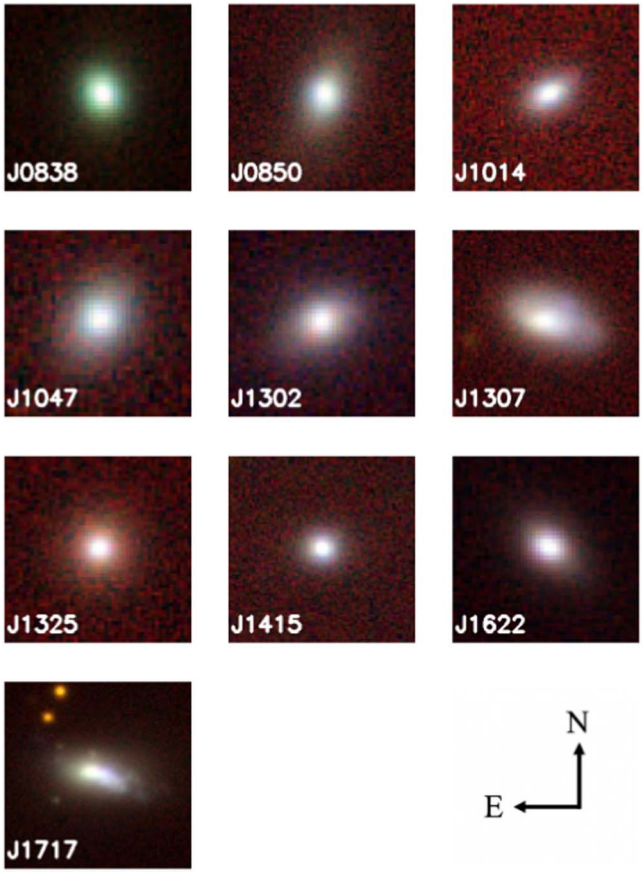

Figure 1. Pan-STARRS (Chambers et al. 2016) color images of the SF dwarfs, generated using the PS1 Image Cutout Server by combining images from the *y*, *i*, and *g* filters. Each image is scaled to 10 kpc on a side.

2. Sample, Observations, and Data Reduction

2.1. Sample

Our goal was to build a suitable control sample to use for comparison to the study of L20. Thus, we targeted SF dwarf galaxies with similar redshift and stellar mass that have prominent outflows but no signs of AGN activity.

To obtain this sample, we selected all galaxies from the NASA–Sloan Atlas with $M_* < 10^{10}$ $M_\odot$ and $z < 0.05$ that were optically classified by the Sloan Digital Sky Survey (SDSS) as an SF or starburst galaxy. We then used the open-source Python code Bayesian AGN Decomposition Analysis for SDSS Spectra (BADASS; Sexton et al. 2020) to fit the SDSS spectra of these galaxies in order to search for broad components to the [O III] λ5007 emission lines, which are indicative of outflow activity. Only 72 out of 26,560 galaxies (0.27%) showed significant broad components, a fraction consistent with that found in samples of more massive galaxies (Matzko et al.

Table 1
Properties of the Targets and Summary of Observations

Name	Short Name	Redshift	$\log(M_*/M_\odot)$	R_{50} (kpc)	$\log(L_{[O\ III]})$ (erg s^{-1})	t_{exp} (s)	PSF ($''$)	PA (deg)	SFR ($M_\odot$ yr^{-1})
(1)	(2)	(3)	(4)	(5)	(6)	(7)	(8)	(9)	(10)
SDSS J083841.97+354350.0	J0838	0.041	9.13	0.86	40.63	2 × 1200	0.83	4.5	0.5
SDSS J085024.95+294051.8	J0850	0.026	9.35	1.10	40.05	3 × 900	0.85	339.6	0.1
SDSS J101440.21+192448.9	J1014	0.028	8.56	0.81	39.82	3 × 1200	0.83	−57.6	0.1
SDSS J104733.80+222400.5	J1047	0.048	9.59	1.14	39.84	4 × 1200	0.85	321	0.2
SDSS J130240.05+423825.2	J1302	0.043	9.42	1.50	40.26	3 × 1200	0.86	299.3	0.4
SDSS J130724.63+523715.2	J1307	0.026	9.1	1.21	40.11	4 × 900	0.86	74	0.3
SDSS J132532.34+315333.1	J1325	0.037	9.37	1.00	39.77	3 × 1200	0.85	0	0.1
SDSS J141525.26+045602.4	J1415	0.024	9.11	0.59	39.70	3 × 900	0.86	97.5	0.1
SDSS J162244.78+323933.0	J1622	0.041	9.48	0.96	40.41	2 × 900	0.85	44.3	0.4
SDSS J171759.66+332003.8	J1717	0.015	9.85	1.00	40.26	7 × 600	0.86	68	0.3

Notes. Column (1): SDSS name of the target. Column (2): short name of the target. Column (3): redshift of the target taken from SDSS. Column (4): stellar mass taken from the MPA-JHU catalog (Kauffmann et al. 2003). Column (5): half-light radius measured as the Petrosian half-light radius, taken from SDSS. Column (6): total [O III] λ5007 luminosity based on the observed total [O III] λ5007 fluxes added from spaxel to spaxel in KCWI data without extinction correction, in units of ergs per second. Column (7): exposure time of the observation in seconds. Column (8): FWHM of the point-spread function (PSF) from the spectrophotometric standard star, measured in arcseconds. Column (9): position angle of the integral field unit (IFU) in degrees measured east of north. Column (10): star formation rate (SFR) measured from the extinction-corrected [O II] fluxes using the equation given in Kewley et al. (2004).

2022). From this, we selected a subset with the most visible broad [O III] λ5007 components and observed 10 of these targets (shown in Figure 1 and listed in Table 1) with the Keck Cosmic Web Imager (KCWI). These included three targets from the Manzano-King et al. (2019) SF dwarf sample. The targets were matched in redshift and stellar mass to those of L20 (their distributions are shown in Figure 2) and were classified as SF in the Baldwin, Phillips & Terlevich (BPT) diagram (Baldwin et al. 1981; Veilleux & Osterbrock 1987; see Figure 3), which is the diagnostic diagram used to distinguish between AGNs and SF galaxies based on the ratios of optical emission lines. The SF dwarfs are also similar in size to the AGN dwarfs if we compare them based on their half-light radius (average radius of 1.1 kpc for the AGN dwarfs versus 1.0 kpc for the SF dwarfs).

2.2. Observations

All the targets were observed with KCWI (Morrissey et al. 2018) through the Keck program 2021A-U080 (PI: G. Canalizo) on 2021 March 19 and 2021 March 20. All targets were observed using the blue grating (BL), which covers a wavelength range of 3500 to 5500 Å, and the small slicer setup (spectral resolution ∼80 km s^{-1} FWHM at 4550 Å). The observations were obtained under clear sky conditions and a typical seeing of ∼0.″8.

The PSF of these IFU observations was measured using observations of the spectrophotometric standard stars that were taken before and after the on-target observations throughout the night. We stacked narrowband images in the range of 5000–5100 Å and fit 2D Moffat profiles (Moffat 1969) to them. We used a Moffat profile as opposed to the Gaussian profile used by L20, as a Moffat profile fits the radial profile of the star better, as referenced by previous studies (Li et al. 2016). Moreover, there was no significant difference in the FWHMs obtained from both profiles, so we adopted the median FWHM obtained from the best-fit Moffat profiles. There would be some discrepancy in the PSF as we could not take observations of the standard stars at the same time as the science target, but the seeing (as measured by the Maunakea Weather Center) ranged from 0.″75 to 1.″0 across both nights, and the FWHM we measured was well within this range.

2.3. Data Reduction

All the targets were reduced with the KCWI Data Extraction and Reduction Pipeline (KDERP),[10] following the standard procedures listed in the manual. The pipeline also included both wavelength and flux calibrations. We then used routines from the IFSRED (Rupke 2014a) library to resample the cubes with square spaxels as individual exposures had rectangular spaxels. The data cubes were resampled to 0.″15 ×0.″15 using `IFSR_KCWIRESAMPLE`, and then the data cubes of the same target were median-combined into a single data cube using `IFSR_MOSAIC`, which also corrected for shifts caused by dithering.

3. Analysis

3.1. Binning

We spatially binned the data cubes using the Voronoi binning method (Cappellari & Copin 2003). Binning is a useful technique that can be used to preserve the spatial resolution of the data while obtaining a higher signal-to-noise ratio (S/N). This would help us to accurately characterize the broad components in the emission lines to determine the outflows, which might otherwise be missed due to a lower S/N. The Voronoi binning method, in particular, bins or divides the data into hexagonal bins, so data from neighboring pixels are grouped as one to achieve the target S/N. Thus, the size of the bins increases with the distance from the photocenter of the target to match the required S/N. We set an S/N of 5 for our targets as we found that was the highest S/N we could obtain before we started losing spatial information from the binning. All subsequent analysis was done on the Voronoi-binned spectra.

[10] https://github.com/Keck-DataReductionPipelines/KcwiDRP/blob/master/AAAREADME

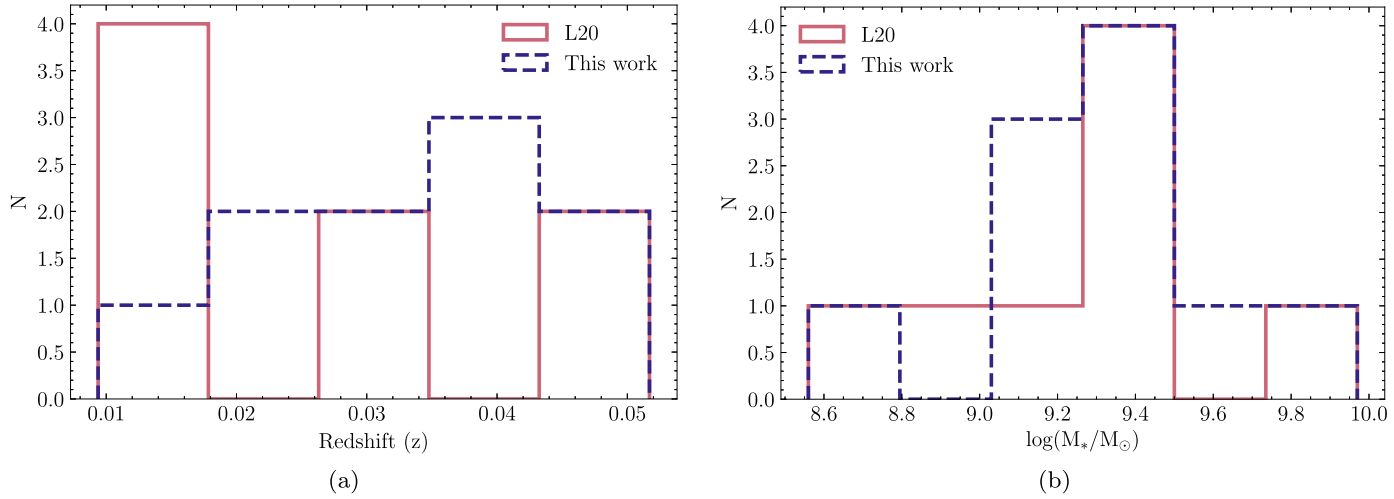

Figure 2. Redshift and stellar mass diagrams comparing the AGN dwarfs from L20 to the SF dwarfs to show that the two samples are matched in stellar mass and redshift. The pink line refers to the sample of dwarfs hosting AGNs while the indigo dashed line refers to the SF dwarfs.

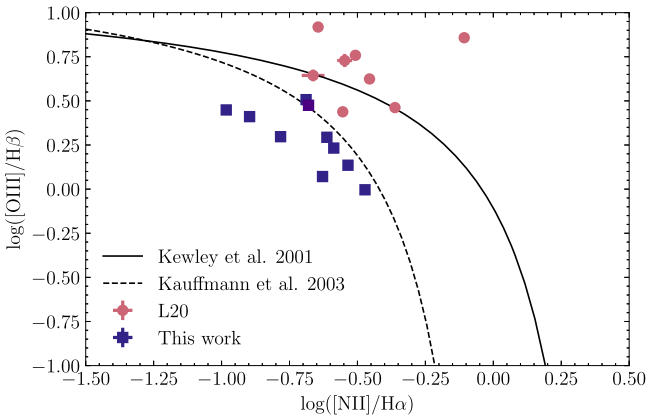

Figure 3. BPT diagram showing the location of targets from the L20 sample of dwarfs hosting AGNs and our sample of SF dwarfs. The line ratios were measured from the SDSS spectra. For most targets, the error bars are smaller than the marker size. The two SF dwarf targets that lie on the boundary within the composite region are J0838 and J0850.

3.2. Spectral Fits

3.2.1. Fitting the [O III] Emission Lines

We first masked the emission lines in the range between 4800 and 5500 Å in order to fit the stellar continuum using the public software pPXF (Cappellari & Emsellem 2004; Cappellari 2017) with the 0.5× solar metallicity stellar population synthesis models from González Delgado et al. (2005). The emission line profiles were mostly symmetric, with no obvious signatures of blueshifted wings. In contrast, most of the broad components of the emission line profiles in L20 were blueshifted.

After subtracting the continuum, we fit the [O III] λλ4959, 5007 emission lines with Gaussian components using the IDL library MPFIT (Markwardt 2012). The line centers of the velocities and widths of both lines were tied together, and only the amplitudes were allowed to vary. We also did not fix the doublet ratios in [O III] in order to allow fits even when a Gaussian component was only detected in one of the two emission lines. We initially tried three different sets of fits. First, we allowed only a maximum of one component, then we allowed a maximum of two, and the final set of fits comprised a maximum of three components. We then used an F-test (described in Section 3.2.2) to choose the number of components to fit the [O III] emission lines.

3.2.2. F-tests to Determine the Optimum Number of Components to Fit the [O III] Emission Lines

The F-test determines the significance of the fit between a complex (higher-order) and a simple (lower-order) model in order to justify the number of Gaussian components we include in our fit. To do this, we calculated the standard deviation of the residuals of the fit (given by σ) for each spaxel. We did the F-test, given as $F = (\sigma_{\rm lower-order})^2/(\sigma_{\rm higher-order})^2$, for one versus two components as well as for two versus three components for the Gaussian fits to the [O III] λλ4959, 5007 lines. The F-test was calculated over a wavelength range of 4800–5500 Å, which includes the [O III] λλ4959, 5007 lines. An F value greater than 3 indicates that the higher-order fit (i.e., the fit using more components) is justifiable. We performed the F-test for the fits to the [O III] λλ4959, 5007 lines in every spaxel of our targets and mapped the results of the F-test. All targets failed the F-test for one component, so more than one component was required to fit the profile. For some of the targets (J1325, J1622, J1047, and J1014), it was evident that we needed only two components. The rest of the targets were more ambiguous since they contained a fraction of spaxels with F values close to, but below, 3. For those targets, we inspected the fits visually to assess the effect that including an additional component had on the residuals and to determine whether the additional component was fitting a real feature in the emission lines. From Figure 4(a), we see that fitting a single component is not sufficient, and it misses a crucial part of the emission line. In Figure 4(c), we see that the third component does not fit any real feature. We, therefore, chose to use a maximum of two components (Figure 4(b)) for all the targets to keep the fits as simple as possible, with the caveat that our flux measurements may miss a small fraction in the wings of the emission lines. This is also different from the analysis of L20, in which three of the eight targets needed three components to get the best fit, while two needed just one component.

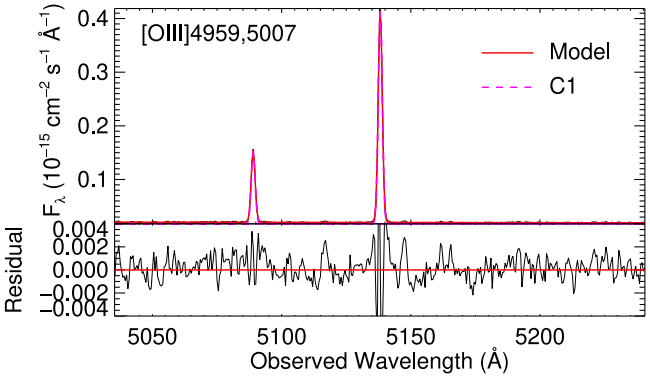

(a) 1 component fit

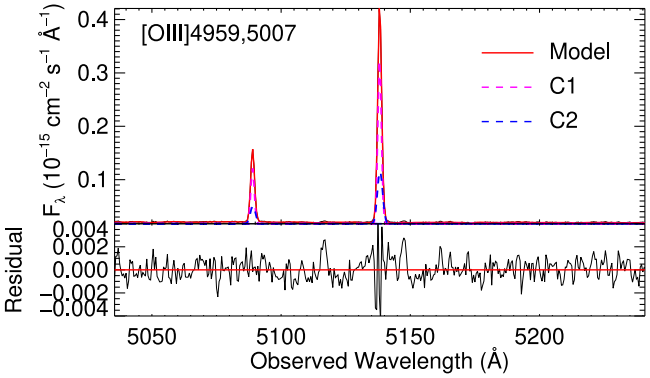

(b) 2 component fit

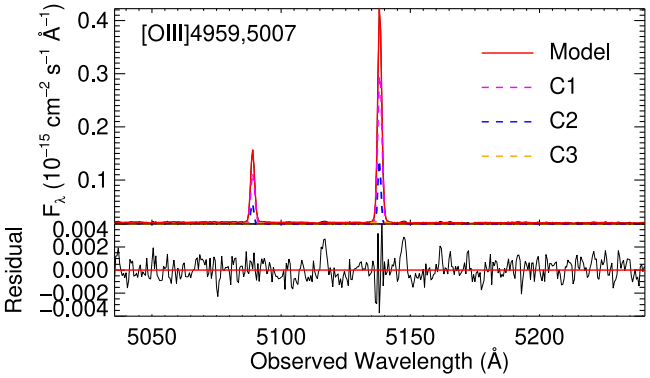

(c) 3 component fit

Figure 4. Examples of (a) one Gaussian component, (b) two Gaussian components, and (c) three Gaussian components fit to the [O III] doublet line profile for J1307 in the same single spaxel. In each panel, the black spectrum is the observed data, the solid red line is the best fit, and the dashed curves represent the Gaussian components. The residuals after subtraction from the best fit are shown at the bottom of each panel. The single component in (a) does not fit the wings accurately, while the third component in (c) does not improve the fit significantly.

3.2.3. Fitting the Full Spectrum

After obtaining robust fits to the [O III] $\lambda\lambda$4959, 5007 emission lines, we fit the emission lines to the entire spectral range and simultaneously fit strong emission lines such as Hβ, Hγ, Hδ, [O II] $\lambda\lambda$3726, 3729, and [Ne III] λ3869. Following the results of the *F*-test for the [O III] $\lambda\lambda$4959, 5007 lines, a maximum of two components were fit for these lines.

3.3. SFRs

The SFRs of the SF dwarfs were calculated from the [O II] lines using the following equation (Kewley et al. 2003):

$$\mathrm{SFR}[M_\odot\ \mathrm{yr}^{-1}] = \frac{7.9 \times 10^{-42} L[\mathrm{O\ II}](\mathrm{erg\ s}^{-1})}{(-1.75)[\log(\mathrm{O/H}) + 12] + 16.73} \quad (1)$$

where [log(O/H) + 12] was taken to be 8.9 for solar metallicities (as adopted by L20). If we consider a 0.5× solar metallicity, the SFR would be ∼30% lower.

These values are listed in column (10) of Table 1. We find that for most of our targets, the SFR is higher than the values listed for the AGN dwarfs from L20, which have an average upper limit of 0.20 $M_\odot$ yr^{-1}. In comparison, the average for the SF dwarfs is 0.25 $M_\odot$ yr^{-1}. We note that the SFR values for the SF dwarfs are likely to be higher than those for the AGN dwarfs, as there could be a significant contribution from the AGN to the [O II] emission lines, which in turn could lead to an overestimation of the value of the SFR.

The SFR for 9 of the 10 objects in our sample could also be obtained from the MPA-JHU catalog, in which the SFRs were calculated based on the techniques used in Brinchmann et al. (2004). These values are much higher than our calculated values, with an average of 1.38 $M_\odot$ yr^{-1}. This could be because the MPA-JHU estimates used multiple lines as SF indicators, while we only used the [O II] lines for our estimates. The biggest difference was for J0838, which had an MPA-JHU estimate for the SFR of 3.94 $M_\odot$ yr^{-1} as compared to the SFR of 0.45 $M_\odot$ yr^{-1} we measured from [O II].

4. Outflows Detected in the Sample

4.1. Gas Kinematics

We calculated the median, minimum, and maximum values of v_{50} and W_{80} for the emission lines in our targets, similar to the methodology adopted by L20 for AGN dwarfs. The parameter v_{50} is defined as the median velocity at the 50th percentile of the total flux, while W_{80} is the line width that includes 80% of the total flux. W_{80} was calculated as $v_{10} - v_{90}$, where v_{10} and v_{90} are the velocities at the 10th and 90th percentiles of the flux, calculated from the red side of the line. For a schematic diagram depicting the different quantities mentioned, refer to Figure 3 in L20.

These values were determined relative to the systemic velocity of the galaxy, which we determined by fitting stellar absorption features in the integrated spectrum of the data cube. Uncertainties in the velocity measurements were estimated by Monte Carlo methods over 100 iterations.

Measurement uncertainties in v_{50} estimated in this way are typically below 5 km s^{-1}. However, velocity maps (see Figure 5) show bin-to-bin variations in the order of 20 km s^{-1} in some cases. These fluctuations are more likely to be due to error measurements than to true changes in velocity. Therefore, we adopted 20 km s^{-1} as a conservative error in our velocity measurements. Our measurements for the whole sample are summarized in Table 2.

A maximum of two components were fit to the emission lines for each of the targets. The C1 component refers to the narrow component, and C2 refers to the broad component. L20 assumed that C2, or in some cases C3, refers to the outflow component since nearly all of their C2/C3 v_{50} values were blueshifted, which is a clear indicator of

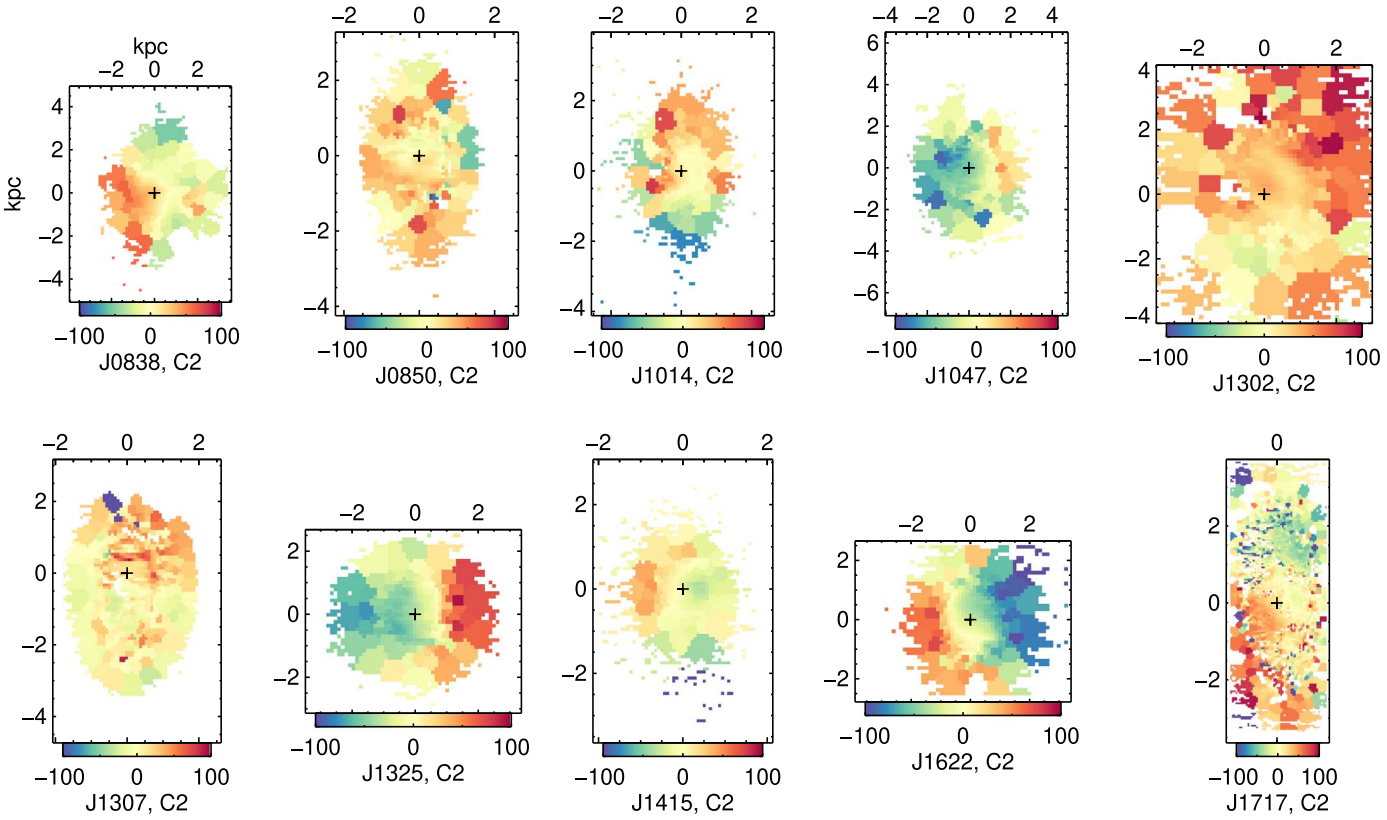

Figure 5. Velocity maps with the v_{50} of the C2 component measured in kilometers per second for all the SF dwarfs. The extent of the outflows in kiloparsecs is indicated by the x-axis and y-axis. The black cross indicates the center of the galaxy. Measurement errors for individual values of v_{50} range between 1 and 5 km s^{-1}. However, velocity variations from bin to bin indicate that the true uncertainty is closer to 20 km s^{-1}.

outflows. In our case, the broad components were approximately at the systemic velocity or even redshifted, with only certain regions showing significantly blueshifted velocity (Figure 5). We only considered spaxels with a blueshifted velocity relative to the systemic to constitute an outflow. Redshifted values of the C2 v_{50} could indicate disturbed or stirred gas in the galaxy. If we had chosen redshifted spaxels to constitute the outflows as well, then that would have indicated a larger fraction of the spaxels contributed to outflowing material, which could change the values of the energetics carried out by the flow. This could lead to either overestimation or underestimation of the effect of the outflow. Since we did not have a good indicator to determine whether the redshifted spaxels truly constituted an outflow, we tended to agree with the generally used assumption that only blueshifted spaxels are likely to depict an outflow. However, for completeness, we considered both cases (using blueshifted spaxels versus using both blue- and redshifted spaxels) in our analysis of the energetics of the outflows (see Section 4.8).

On average, the median values of v_{50} for the C2 component were close to 0 km s^{-1}. This could be due to the fact that most of the spaxels did not have a significant velocity offset. However, since we considered only blueshifted velocity values to constitute the outflows, the average of the minimum (maximally blueshifted) values of v_{50} was found to be ~ -60 km s^{-1}. From the velocity maps in Figure 5, we see that blueshifted outflows constitute a small fraction of the kinematics in the galaxy. The C2 W_{80} velocity maps are plotted in Figure 6 and show a significant spread in the dispersion values. The average of the median values of W_{80} was $\sim$480 km s^{-1}.

As mentioned earlier, the shape of the line profile of the broad component in our targets is not preferentially blueshifted and is symmetric, in contrast to the clear blueshifted line profile in L20's AGN dwarfs. This is consistent with previous observations of line profiles associated with star-formation-driven outflows (Concas et al. 2017; Davies et al. 2019; Matzko et al. 2022). The symmetric shape of the line profiles in the SF dwarfs could indicate lower extinction along the line of sight in at least some of the outflows. AGN-powered outflows originate from the dusty centers of galaxies, and so they are affected by extinction, which would lead to their profiles being more blueshifted (Heckman et al. 1981). However, stellar-driven outflows are not restricted to originating from the centers of galaxies, as energetic stellar processes can occur anywhere in the galaxy. Any outflows near the edge of galaxies, i.e., those that are least affected by extinction, are more likely to dominate the flux of the final spectrum, leading to a profile that appears to be more symmetric, with velocity values centered around 0 km s^{-1} (S. Kadir et al. 2023, in preparation).

4.2. Gas and Stellar Kinematics

We plot the v_{50} maps for the C1 component and the stellar fields in Figures 7 and 8, respectively. The C1 component represents the gas that follows the stellar component in the galaxy. Comparing Figures 5 and 7, we see that for nearly all the targets, the C1 and C2 components have distinct kinematics, implying that the two components are likely

Table 2
Kinematic Properties of the Targets

Name	N_{comp}	Component	Median v_{50} (km s^{-1})	Min v_{50} (km s^{-1})	Max v_{50} (km s^{-1})	Median W_{80} (km s^{-1})	Max W_{80} (km s^{-1})
(1)	(2)	(3)	(4)	(5)	(6)	(7)	(8)
J0838	2	C2	−5	−53	61	397	625
		C1	15	−2	69	113	180
		Total	16	−7	54	315	474
J0850	2	C2	21	−53	58	593	832
		C1	30	−40	86	124	168
		Total	38	−19	82	278	648
J1014	2	C2	7	−80	62	378	855
		C1	−7	−50	20	87	139
		Total	19	−42	43	127	701
J1047	2	C2	−28	−82	22	651	830
		C1	13	−10	32	118	171
		Total	19	−1	43	522	778
J1302	2	C2	23	−21	122	721	1203
		C1	27	−40	22	130	238
		Total	31	−11	82	551	1042
J1307	2	C2	9	−20	50	385	385
		C1	15	−54	60	67	98
		Total	8	−32	71	131	369
J1325	2	C2	−12	−66	72	586	760
		C1	3	−8	26	117	154
		Total	12	−11	35	453	649
J1415	2	C2	−4	−41	41	488	641
		C1	5	−12	42	122	152
		Total	12	−61	42	318	586
J1622	2	C2	−20	−93	58	462	671
		C1	−12	−58	99	122	162
		Total	−14	−57	62	246	395
J1717	2	C2	10	−77	100	178	725
		C1	6	−67	171	79	159
		Total	8	−48	76	139	244

Notes. Column (1): short name of the target. Column (2): number of components used for the fit. Column (3): component number. Columns (4)–(6): median, minimum, and maximum values of v_{50} measured across the cube. Columns (7)–(8): median and maximum values of W_{80} measured across the cube. The spaxels with the highest and the lowest 5% of v_{50} were ignored in the calculations. Measurement errors for individual values of v_{50} range between 1 and 5 km s^{-1}.

tracing different physical processes. For instance, the velocity fields for the C1 and C2 components for J1622 in Figures 5 and 7 are perpendicular to each other, possibly indicating that the outflow is oriented perpendicularly to the rotation of the galaxy. As mentioned earlier, the gas in the C1 component follows the stellar component in the galaxy as can be readily seen by comparing Figures 8 and 7. We see signs of rotation in the stellar field of some targets such as J1047, J1307, J1622, and J1717. For the rest of the targets, there does not seem to be a clear rotation in the stellar velocity, indicating that either we are seeing the galaxies face-on in some cases, or the galaxies may not be supported by rotation in other cases.

The W_{80} velocity maps of the C1 component of J1325 in Figure 9(a) show narrower widths of the line profile compared to those of the C2 component. This trend was prevalent among all objects in the sample, possibly indicating that the C2 component likely traces processes like outflows that can cause the broadening of the line profiles, while the C1 component is relatively quiescent. We refer the reader to the appendix for a more detailed analysis of the v_{50} and W_{80} maps of the C1 and C2 components of the individual targets. The stellar velocity dispersion of all the targets also has low values as indicated by Figure 9(b).

4.3. Spatial Extent and Radial Profiles of the Broad Component

Figure 5 also shows the spatial distribution of the C2 component for each galaxy, with the axes in units of kiloparsecs. The outflows appear to extend to significantly larger radii than the half-light radius of these targets as given by SDSS (see Table 1). We also mapped the radial profile of the outflows and compared it to the PSF (see Appendix B). We fit a Moffat profile to a standard star that was observed close to the target to reduce uncertainties caused by changes in atmospheric turbulence and to determine the physical extent of the outflows in our targets. The deviation from the

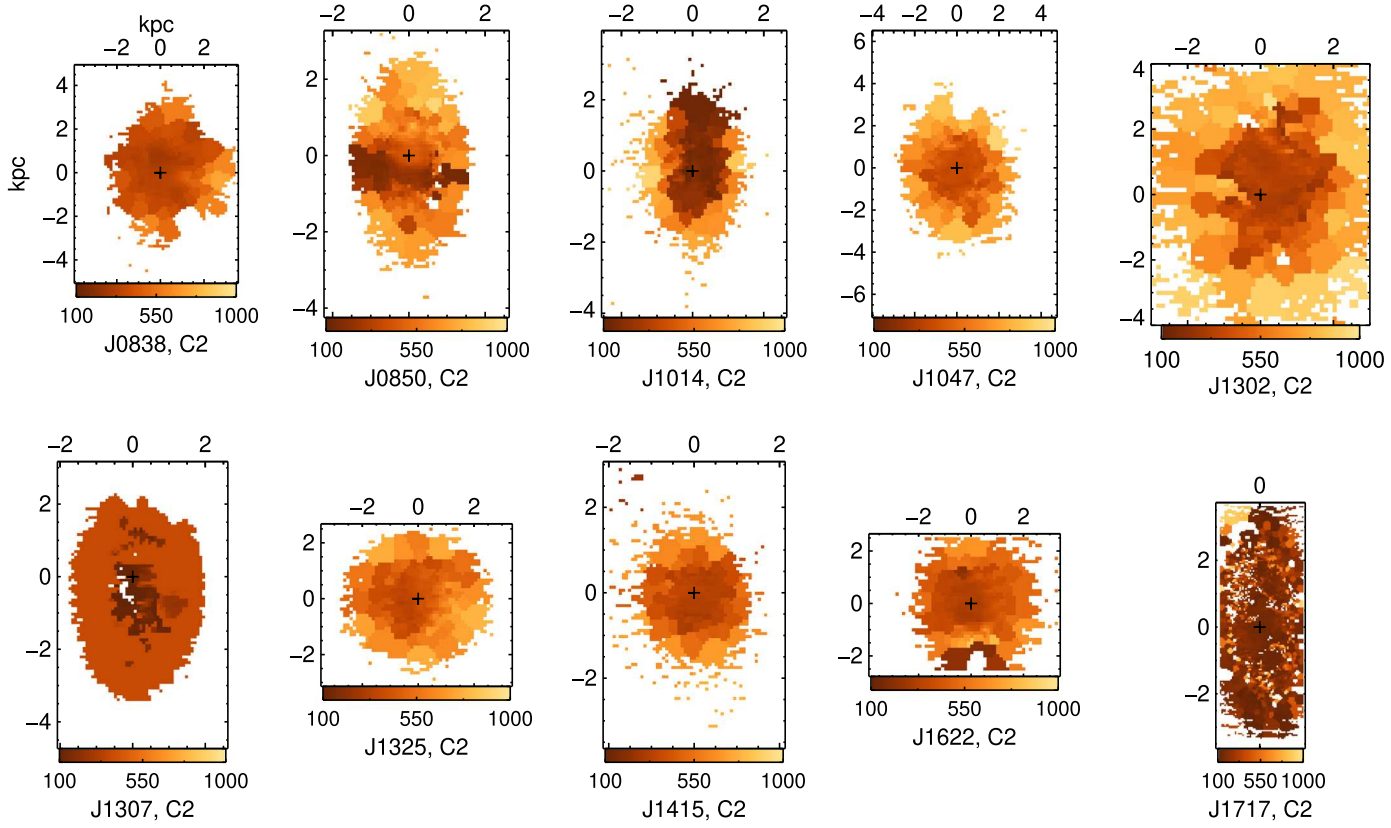

Figure 6. W_{80} maps showing the width of the velocity profile in kilometers per second of the C2 component in all the SF dwarfs. Measurement errors for W_{80} range from 2 to 10 km s^{-1}. There is a large range in dispersion values, with a median W_{80} of ∼480 km s^{-1}.

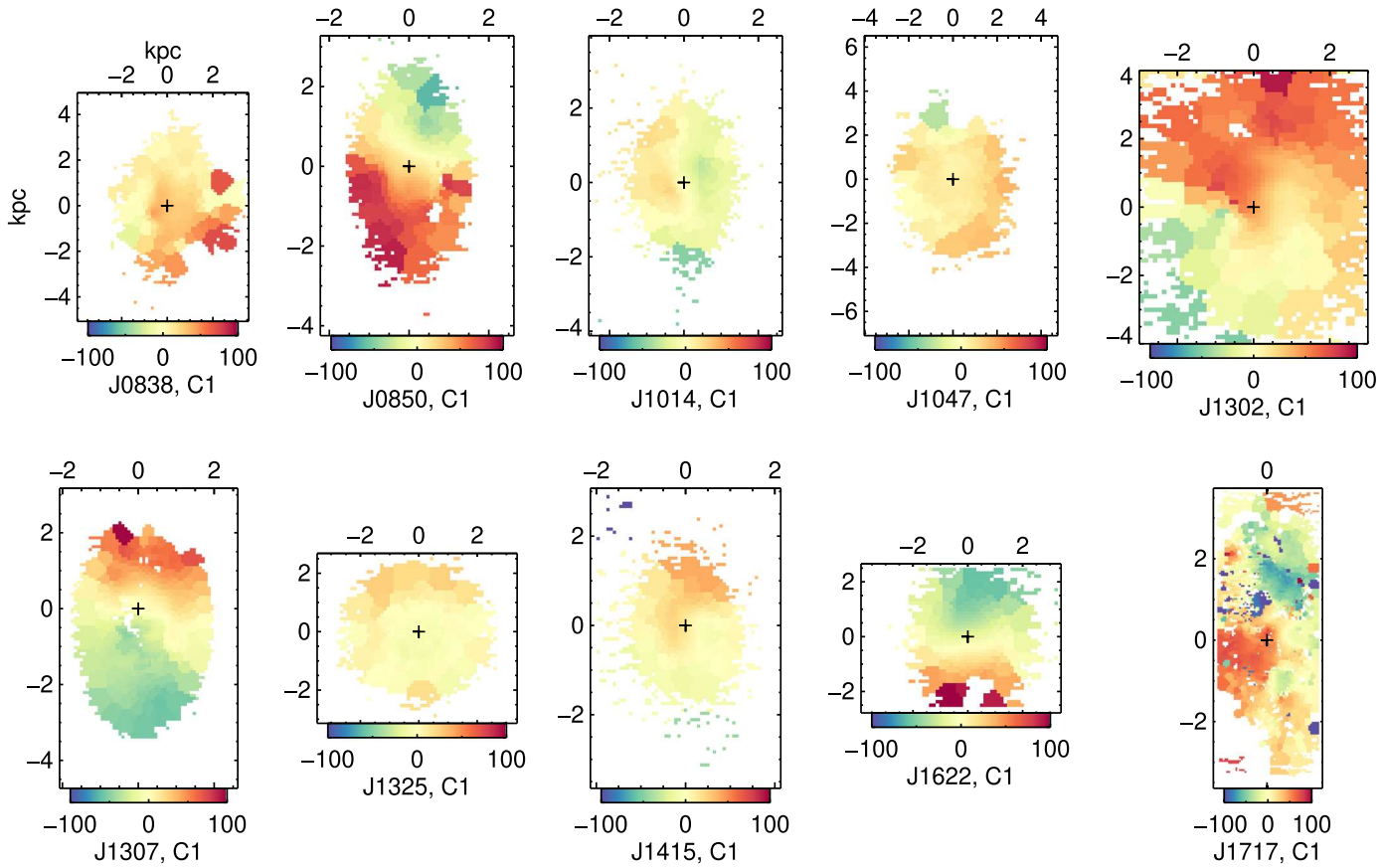

Figure 7. Velocity maps with the v_{50} of the C1 component measured in kilometers per second for all the SF dwarfs.

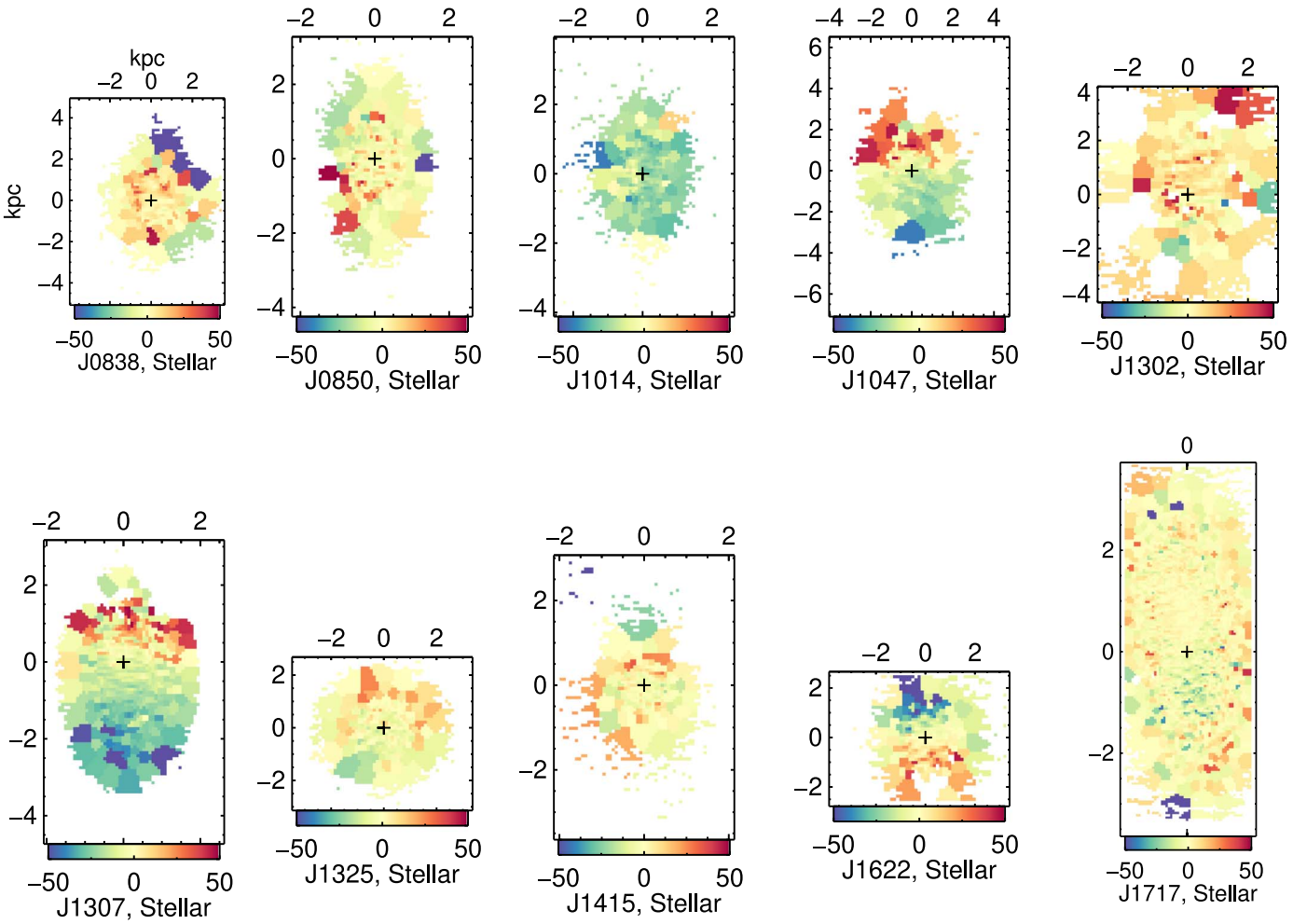

Figure 8. Velocity maps with the v_{50} of the stellar component measured in kilometers per second for all the SF dwarfs.

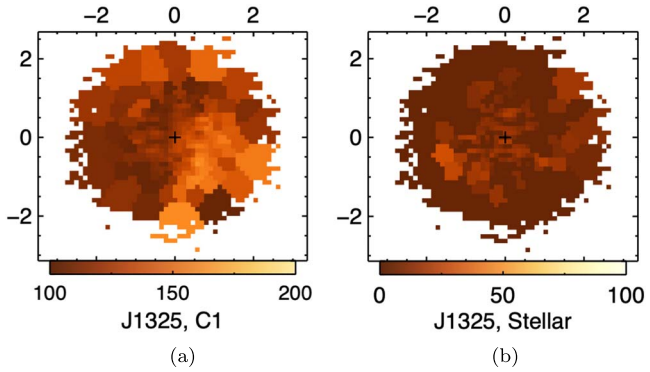

Figure 9. Example of the distribution of W_{80} for (a) the C1 component and (b) the stellar velocity dispersion (σ) for J1325. The rest of the targets have similar W_{80} and σ maps indicating minimal dispersion, in contrast to the W_{80} maps of the C2 component.

profile of the star for all the targets shows that the outflows are spatially extended.

4.4. Multiple H II Regions

The [O III] λ5007 flux maps of our targets show that multiple H II regions are present in some of the targets (see Figures 19 and 23). These are most apparent in J1307 and J1717, but they are also likely present in J0838, J0850, J1014, and J1302. This makes it challenging to set a single radius for the outflow while determining the energetics (see Section 4.8), since different regions may have outflows of different sizes. L20 used a single spherical shell model for their sample of AGN dwarfs as AGN-powered outflows originate from a central source and the morphology of the outflows is spherical on the 2D sky plane. For comparison purposes, we considered a similar spherical shell model for the SF dwarfs. The radius of the outflow was taken to be the extent to which the outflow component could be measured from the radial profiles and velocity maps. Thus, the results need to be analyzed with caution since the radius of the outflows could be much smaller.

4.5. Outflow Ionization: [O III]/Hβ Ionization Maps

Since our main goal was to compare outflows powered by star formation to those powered by AGNs, it was important to make sure the galaxies in our sample do not host any AGN activity. The targets in our sample were classified as SF based on integrated SDSS spectra (Figure 3). However, a weak AGN signal could be diluted by the strong emission lines associated with SF regions.

Using MaNGA IFU data, Mezcua & Domínguez Sánchez (2020) found AGN activity in individual spaxels based on the ionized line ratios of lines used in the BPT diagram that was not apparent in the integrated spectra of the same targets. We took a similar approach for our data cubes to ensure that all of

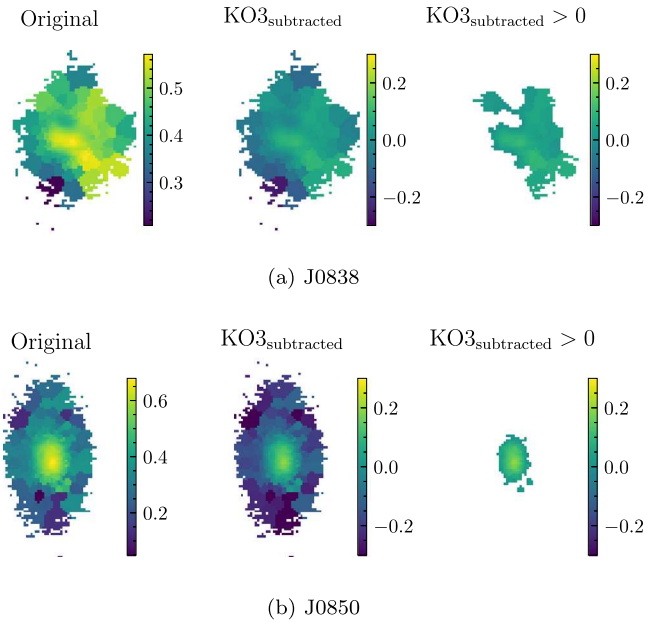

Figure 10. Ionization test maps for (a) J0838 and (b) J0850. The first panel in each row is the actual [O III]/Hβ flux map, and the second panel is the flux map after subtraction of the expected [O III]/Hβ value. The third panel shows if any part of the galaxy has an [O III]/Hβ line ratio in the composite region. For both (a) and (b), some parts have a higher line ratio than expected for SF regions from the BPT diagram. These two are the only targets in the sample with signatures of potential AGN contamination.

the ionization is likely caused by SF activity and to rule out any possibility of AGN activity that can manifest itself in the various comparison ratios.

To do this, we obtained the [O III]/Hβ ratio for each spaxel and compared it to the value of the Kauffmann demarcation line (KO3; Kauffmann et al. 2003) between AGN and SF galaxies. We chose the Kauffmann demarcation line because it has lower limits than the Kewley line (Kewley et al. 2001). Since the KCWI wavelength coverage does not extend beyond 5500 Å, we were unable to measure the [N II]/Hα ratio directly. So for each target, we obtained the value of [N II]/Hα from SDSS and determined the corresponding [O III]/Hβ ratio on the Kauffmann line. Note that this value of [N II]/Hα was obtained using an integrated aperture and thus may not be indicative of the actual spaxel-to-spaxel variation of the line ratio. This could lead to the biasing of the ratio toward the center of the galaxy and to significant errors while determining values in outer regions. Being mindful of this caveat, we subtracted the obtained value from our calculated value and plotted those spaxels where the difference was greater than 0 (see Figure 10). If the difference is greater than 0, the ratio is higher than the accepted value for possible SF origins.

For 8 of the 10 targets, no part of the galaxy indicated [O III]/Hβ ratios above the SF line. In two targets, J0838 and J0850, the ratios in some spaxels were 0.2 dex greater than the expected value; Figure 10 shows the specific location of these spaxels. While the higher [O III]/Hβ ratios in these spaxels are likely due to shocks, we cannot rule out the possibility that there may be some AGN contamination in these two targets. However, all the outflow properties in these two targets appear to be consistent with the rest of the sample, so their outflows are most likely powered by star formation.

4.6. Electron Densities

The electron densities of the targets can be obtained from the [S II] line ratios or the [O II] line ratios from the relation given by Sanders et al. (2016). We took the [S II] line ratios from SDSS for all our targets (similar to L20). The values of the electron densities (average value of $\sim$165 cm^{-3}) were lower compared to the values for the AGN dwarfs (average value of $\sim$400 cm^{-3}). This difference between the two samples could have been caused by the fact that AGNs are capable of producing strong ionization and thus have higher values of ionized electron densities than SF dwarf galaxies.

4.7. Dust Extinction

Dust extinction in the targets was measured using the Hβ/Hγ emission line ratios of their integrated spectrum. The extinction was calculated using the extinction curve from Cardelli et al. (1989) with an $R_v = 3.1$ and an intrinsic Hβ/Hγ ratio of 2.13 using case B from Osterbrock & Ferland (2006) at a temperature of 10^4 K. We also compared these values to the extinction calculated from the Hα/Hβ line ratios obtained from SDSS, and they were comparable within the error limits. So we used the values of extinction A_v determined from the Hβ/Hγ ratios for further calculations. The values of the electron densities and extinction for the SF dwarfs are given in columns (3) and (4) of Table 3.

4.8. Energetics of the Outflows

Following L20, the ionized gas masses were calculated using the Hβ luminosity of the outflowing gas. We converted the Hβ luminosity to the Hα luminosity by a correction factor $L_{\mathrm{H}\alpha,\mathrm{corr}} = 2.86\ L_{\mathrm{H}\beta,\mathrm{corr}}$. The correction factor is the intrinsic Hα/Hβ ratio for H II regions, which is appropriate for the case B recombination assumed from Osterbrock & Ferland (2006) with $T = 10^4$ K. We also corrected for extinction based on an intrinsic Hβ/Hγ ratio of 2.13 (for more details, refer to Section 4.7). The equation for the ionized mass was adapted from Equation (29) in Veilleux et al. (2020) by assuming solar metallicity and is given as

$$M_{\mathrm{out}} = 4.48\ M_{\odot}\left(\frac{L_{\mathrm{H}\alpha,\mathrm{corr}}}{10^{35}\ \mathrm{erg\ s^{-1}}}\right)\left(\frac{\langle n_e\rangle}{100\ \mathrm{cm^{-3}}}\right)^{-1}. \quad (2)$$

We also calculated the mass-loss rates (*dM/dt*), the momentum rates in units of energy (*cdp/dt*), and the kinetic energy rates (*dE/dt*). We assumed a time-averaged, thin-shell free wind model, which has been previously used by Shih & Rupke (2010), Rupke & Veilleux (2013b), and L20, with a spherically symmetric outflow.

The energetics were calculated by summing up quantities over individual spaxels:

$$dM/dt = \sum dm/dt = \sum \frac{m_{\mathrm{out}}\, v_{50,\mathrm{out}} \sec\theta}{R_{\mathrm{out}}} \quad (3)$$

$$dp/dt = \sum (v_{50,\mathrm{out}} \sec\theta)\, dm/dt \quad (4)$$

$$dE/dt = \frac{1}{2}\sum [(v_{50,\mathrm{out}} \sec\theta)^2 + 3\sigma_{\mathrm{out}}^2]\, dm/dt, \quad (5)$$

where m_{out} is the outflowing mass in each spaxel, $v_{50,\mathrm{out}}$ is the value of v_{50} in each spaxel, and σ_{out} is the velocity dispersion calculated as $W_{80}/2.73$. R_{out} is the radial extent of the spherical outflow and was determined from the maximum radial extent

Table 3
Energetics of the Outflows

Name	Comp	n_e (cm^{-3})	Extinction ($E(B-V)$)	$\log(M/M_\odot)$	$R_{\rm out}$ (kpc)	$\log[(dM/dt)/(M_\odot\ {\rm yr}^{-1})]$		$\log[(dE/dt)/({\rm erg\ s}^{-1})]$		$\log[(cdp/dt)/(L_\odot)]$	
						Blue	Red+Blue	Blue	Red+Blue	Blue	Red+Blue
(1)	(2)	(3)	(4)	(5)	(6)	(7)	(8)	(9)	(10)	(11)	(12)
J0838	C1	121 ± 0	0.2	$4.4^{+0.2}_{-0.2}$	2.9	$-4.1^{+0.2}_{-0.2}$	$-1.9^{+0.2}_{-0.2}$	$37.0^{+0.2}_{-0.2}$	$37.0^{+0.2}_{-0.2}$	$4.8^{+0.2}_{-0.2}$	$7.4^{+0.2}_{-0.2}$
	C2			$5.9^{+0.2}_{-0.2}$	2.9	$-2.3^{+0.2}_{-0.2}$	$-2.0^{+0.2}_{-0.2}$	$36.7^{+0.2}_{-0.2}$	$34.0^{+0.2}_{-0.2}$	$7.0^{+0.2}_{-0.2}$	$7.4^{+0.2}_{-0.2}$
J0850	C1	150 ± 0	0.2	$5.0^{+0.2}_{-0.2}$	1.2	$-2.8^{+0.2}_{-0.2}$	$-2.0^{+0.2}_{-0.2}$	$36.2^{+0.2}_{-0.2}$	$37.03^{+0.2}_{-0.2}$	$6.5^{+0.2}_{-0.2}$	$7.6^{+0.2}_{-0.2}$
	C2			$4.4^{+0.2}_{-0.2}$	1.2	$-3.5^{+0.2}_{-0.2}$	$-2.5^{+0.2}_{-0.2}$	$35.5^{+0.2}_{-0.2}$	$36.7^{+0.2}_{-0.2}$	$5.8^{+0.2}_{-0.2}$	$6.9^{+0.2}_{-0.2}$
J1014	C1	63 ± 24	0.1	$5.7^{+0.3}_{-0.2}$	2.7	$-1.9^{+0.3}_{-0.2}$	$-2.3^{+0.3}_{-0.2}$	$37.3^{+0.3}_{-0.2}$	$36.2^{+0.3}_{-0.2}$	$7.6^{+0.3}_{-0.2}$	$6.8^{+0.3}_{-0.2}$
	C2			$4.6^{+0.3}_{-0.2}$	2.7	$-1.9^{+0.3}_{-0.2}$	$-2.5^{+0.3}_{-0.2}$	$37.3^{+0.3}_{-0.2}$	$36.2^{0.3}_{-0.2}$	$7.6^{+0.3}_{-0.2}$	$6.7^{+0.3}_{-0.2}$
J1047	C1	265 ± 2	0.2	$3.0^{+0.4}_{-0.3}$	2.0	$-5.1^{+0.4}_{-0.3}$	$-2.4^{+0.4}_{-0.3}$	$33.2^{+0.3}_{-0.3}$	$35.8^{+0.3}_{-0.3}$	$3.9^{+0.4}_{-0.3}$	$7.0^{+0.4}_{-0.3}$
	C2			$2.0^{+0.4}_{-0.3}$	2.0	$-1.8^{+0.4}_{-0.3}$	$-2.7^{+0.4}_{-0.3}$	$37.3^{+0.4}_{-0.3}$	$36.2^{+0.4}_{-0.3}$	$7.6^{+0.4}_{-0.3}$	$6.7^{+0.4}_{-0.3}$
J1302	C1	146 ± 2	0.2	$4.6^{+0.2}_{-0.2}$	2.1	$-3.3^{+0.2}_{-0.2}$	$-2.4^{+0.2}_{-0.2}$	$35.5^{+0.2}_{-0.2}$	$37.1^{+0.2}_{-0.2}$	$6.0^{+0.2}_{-0.2}$	$7.0^{+0.2}_{-0.2}$
	C2			$3.9^{+0.2}_{-0.2}$	2.5	$-4.2^{+0.2}_{-0.2}$	$-2.6^{+0.2}_{-0.2}$	$37.2^{+0.2}_{-0.2}$	$37.2^{+0.2}_{-0.2}$	$5.1^{+0.2}_{-0.2}$	$7.0^{+0.2}_{-0.2}$
J1307	C1	113 ± 15	0.2	$6.0^{+0.2}_{-0.2}$	1.9	$-1.8^{+0.2}_{-0.2}$	$-2.1^{+0.2}_{-0.2}$	$34.6^{+0.2}_{-0.2}$	$36.8^{+0.2}_{-0.2}$	$7.6^{+0.2}_{-0.2}$	$7.2^{+0.2}_{-0.2}$
	C2			$5.2^{+0.2}_{-0.2}$	1.4	$-2.7^{+0.2}_{-0.2}$	$-2.5^{+0.2}_{-0.2}$	$35.7^{+0.2}_{-0.2}$	$37.3^{+0.2}_{-0.2}$	$6.4^{+0.2}_{-0.2}$	$7.2^{+0.2}_{-0.2}$
J1325	C1	233 ± 40	0.1	$5.4^{+0.2}_{-0.2}$	1.6	$-3.0^{+0.2}_{-0.2}$	$-3.2^{+0.2}_{-0.2}$	$34.1^{+0.2}_{-0.2}$	$35.0^{+0.2}_{-0.2}$	$5.5^{+0.2}_{-0.2}$	$5.7^{+0.2}_{-0.2}$
	C2			$5.3^{+0.2}_{-0.2}$	1.5	$-2.2^{+0.2}_{-0.2}$	$-2.8^{+0.2}_{-0.2}$	$35.8^{+0.2}_{-0.2}$	$36.3^{+0.2}_{-0.2}$	$7.1^{+0.2}_{-0.2}$	$6.6^{+0.2}_{-0.2}$
J1415	C1	271 ± 18	0.2	$4.7^{+0.2}_{-0.2}$	1.5	$-3.7^{+0.2}_{-0.2}$	$-3.0^{+0.2}_{-0.2}$	$34.1^{+0.2}_{-0.2}$	$35.9^{+0.2}_{-0.2}$	$5.0^{+0.2}_{-0.2}$	$6.1^{+0.2}_{-0.2}$
	C2			$5.3^{+0.2}_{-0.2}$	1.4	$-2.5^{+0.2}_{-0.2}$	$-3.1^{+0.2}_{-0.2}$	$35.2^{+0.2}_{-0.2}$	$35.3^{+0.2}_{-0.2}$	$6.5^{+0.2}_{-0.2}$	$6.0^{+0.2}_{-0.2}$
J1622	C1	193 ± 5	0.1	$6.0^{+0.2}_{-0.2}$	3.2	$-2.0^{+0.2}_{-0.2}$	$-2.2^{+0.2}_{-0.2}$	$36.7^{+0.2}_{-0.2}$	$36.5^{+0.2}_{-0.2}$	$7.0^{+0.2}_{-0.2}$	$7.0^{+0.2}_{-0.2}$
	C2			$5.8^{+0.2}_{-0.2}$	2.9	$-2.1^{+0.2}_{-0.2}$	$-2.3^{+0.2}_{-0.2}$	$37.2^{+0.2}_{-0.2}$	$37.0^{+0.2}_{-0.2}$	$7.4^{+0.2}_{-0.2}$	$7.2^{+0.2}_{-0.2}$
J1717	C1	85 ± 11	0.2	$5.7^{+0.3}_{-0.3}$	3.4	$-2.4^{+0.3}_{-0.3}$	$-2.0^{+0.3}_{-0.3}$	$37.0^{+0.3}_{-0.3}$	$37.4^{+0.3}_{-0.3}$	$7.3^{+0.3}_{-0.3}$	$7.4^{+0.3}_{-0.3}$
	C2			$5.7^{+0.3}_{-0.3}$	3.0	$-2.4^{+0.3}_{-0.3}$	$-2.4^{+0.3}_{-0.3}$	$38.0^{+0.3}_{-0.3}$	$37.5^{+0.3}_{-0.3}$	$7.4^{+0.3}_{-0.3}$	$7.2^{+0.3}_{-0.3}$

Notes. Column (1): short name of the target. Column (2): component number. Column (3): electron densities measured from the [S II] line ratios from SDSS. Column (4): the extinction values calculated from the Hβ/Hγ measured from the integrated spectrum of the KCWI data. Column (5): ionized gas mass of the outflow. Column (6): outflow radius used in the calculation of the energetics. Columns (7) and (8): the mass-loss rate calculated using only the blueshifted spaxels and both the blueshifted and redshifted spaxels, respectively, to constitute the outflow. Columns (9) and (10): the energy rate calculated using only the blueshifted spaxels and both the blueshifted and redshifted spaxels, respectively. Columns (11) and (12): the momentum rate calculated using only the blueshifted spaxels and both the blueshifted and redshifted spaxels, respectively. The errors in the energetics are dominated by extinction.

Table 4
Escape Fractions of the Targets

Name	$v_{\rm esc}$ (km s^{-1})	$f_{\rm esc}$ (%)
(1)	(2)	(3)
J0838	260	2
J0850	279	0
J1014	213	0
J1047	308	1
J1302	288	1
J1307	255	0
J1325	282	1
J1415	256	1
J1622	294	1
J1717	337	0

Notes. Column (1): short name of the target. Column (2): escape velocity rounded to the nearest whole number. Column (3): escape fraction calculated, rounded to the nearest whole number.

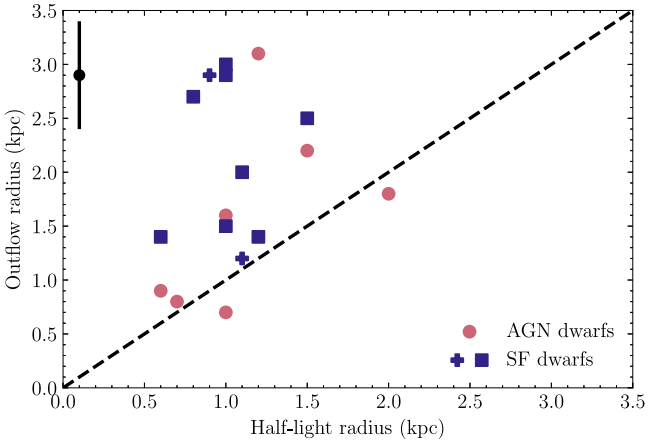

Figure 11. A comparison between the radius of the C2 component (outflow radius) and the half-light radius of the targets. The values of the half-light radius of the SF dwarfs are indicated in Table 1, and the values of the half-light radius of the AGN dwarfs were taken from L20. A cross symbol is used to indicate the two SF targets that could potentially have AGN contamination based on their BPT line ratios; see Section 4.5. The dashed line represents equal values for the outflow radius and half-light radius. The average value of the errors in the data points for the SF dwarfs is indicated by the black symbol.

indicated in the C2 velocity maps of the individual targets (Figures 5 and 6). The angle between the velocity vector of the outflow in 3D space and the line of sight is defined as $\theta = \sin^{-1}(r_{\rm spaxel}/R_{\rm out})$.

The values of the energetics are shown in Table 3. The ionized gas mass in column (5) was calculated using Equation (2) and it gives a measure of the gas moved by the outflows for C2. The values of the energetics in columns (7), (9), and (11) indicate the mass-loss rates, energy rates, and momentum rates of the ionized gas, respectively.

As indicated earlier, we only considered the blueshifted values of $v_{50,\rm out}$ as being part of the outflow. This was added over the entire radial extent to get the total values of the

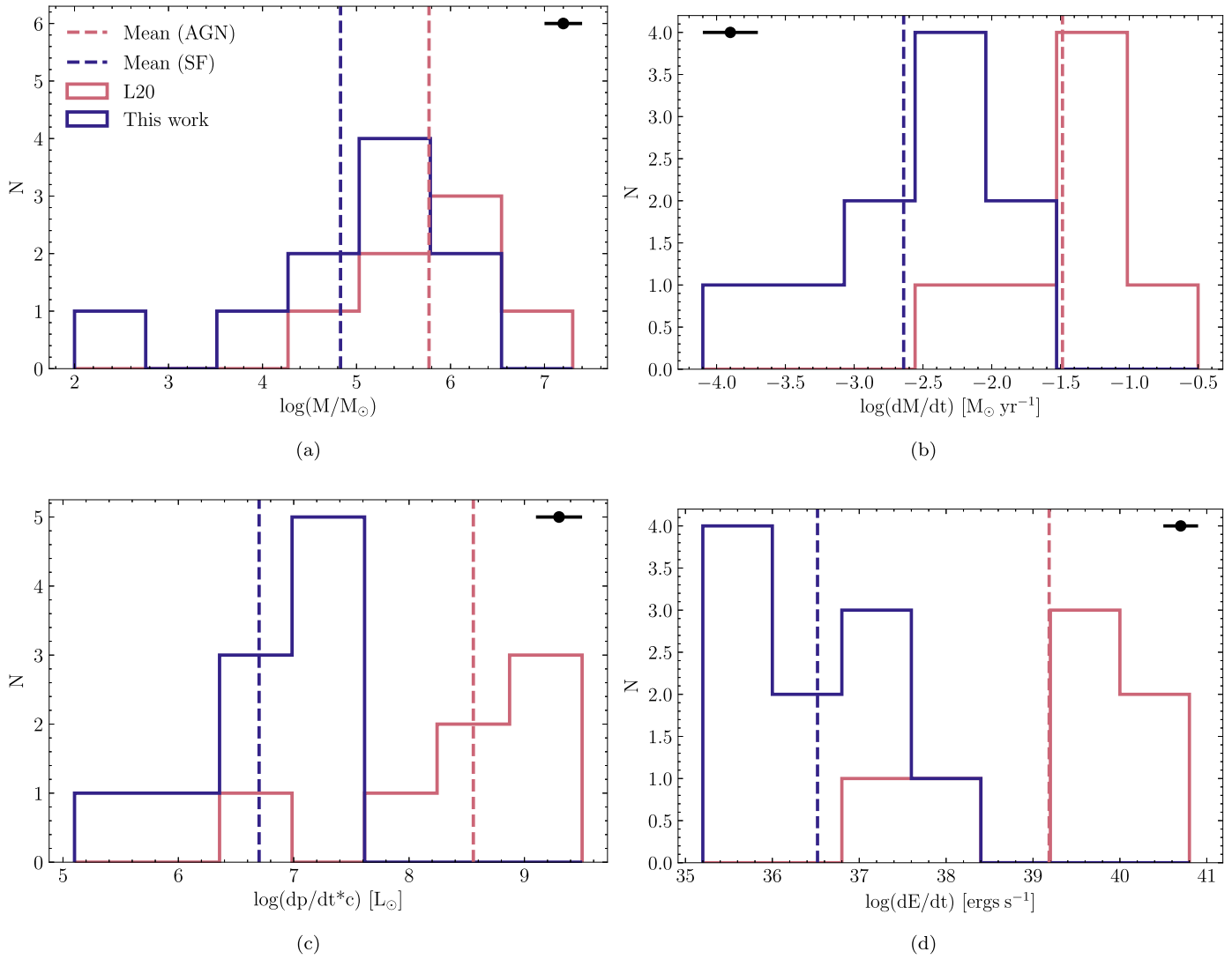

Figure 12. Histograms comparing the energetics of the outflow component calculated in AGN dwarfs and SF dwarfs. Figure 12(a) compares the mass contained in the outflow, and Figures 12(b), (c), and (d) compare the outflow rates of mass, momentum, and kinetic energy, respectively. The dashed lines represent the median value of either sample. The values for the SF dwarfs across all the energetics are lower than those for the AGN dwarfs. The average value of the errors in the data points for the AGN and SF dwarfs is indicated by the black symbol.

energetics. If we also include the redshifted spaxels to constitute the outflow, we find that the value of dE/dt is on average 10% larger than the values calculated for only the blueshifted spaxels, implying that there would be a small increase in the values of the energetics. The values of the energetics calculated by considering both redshifted and blueshifted spaxels to constitute the outflow are given in columns (8), (10), and (12) of Table 3 for comparison.

Comparison of the values given in Tables 2 and 3 to the SFRs in Table 1 shows that there is no correlation between the SFR (or specific SFR) and outflow properties for SF dwarfs. However, this could be due to the poor constraints we have on SFRs, as noted in Section 3.3.

4.9. Does the Outflowing Gas Escape the Galaxy?

As in the analysis done by L20, we compared the outflow velocities of our sample of SF dwarfs to the escape velocities of the galaxies in order to determine whether a significant fraction of the outflowing gas escapes the galaxy.

While there are several methods to calculate the escape velocities of galaxies, we used abundance matching in order to obtain results that can be compared directly to those of L20. We calculated the escape velocities by first obtaining the halo masses of the galaxies using abundance matching (Moster et al. 2013). We assumed a Navarro–Frenk–White dark matter density profile (Navarro et al. 1996). Using the integrated spectrum of the broad component of [O III] λ5007 for each galaxy, we found the ratio of the flux that has velocities higher than the escape velocity to the total flux of the line, and we defined this as the escape fraction. The escape fraction in percentage for the SF dwarfs is given in Table 4. Note that we defined the escape fraction based on the flux ratios, not on the mass ratios, so the caveats listed in L20 still apply here. Our escape velocities were also measured from the center of the galaxy and should be considered conservative upper limits, as escape velocities are highest at the center.

The escape fractions listed in Table 4 demonstrate that only a small fraction of the gas (if any) is able to escape the

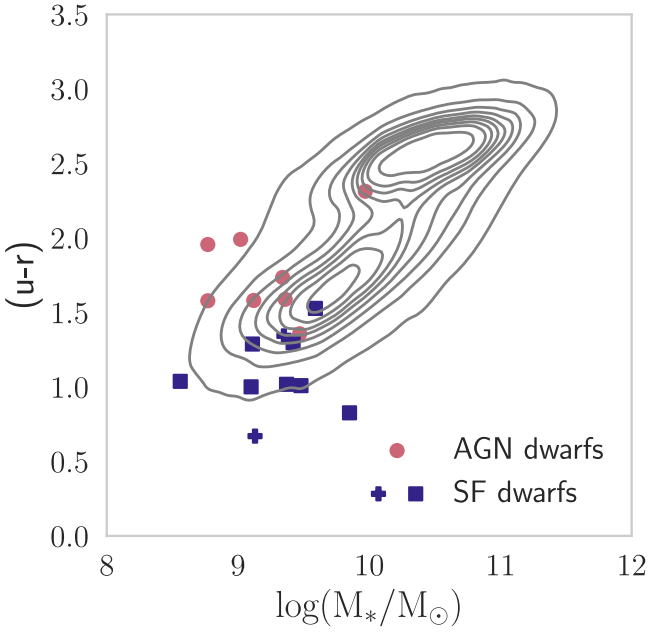

Figure 13. The $u - r$ model magnitude colors from SDSS DR16 are plotted against the MPA-JHU stellar mass. The colors are corrected for galactic extinction following Schlegel et al. (1998) and the contours are from Schawinski et al. (2014). The cross symbols for the SF dwarfs are again used to specify J0838 and J0850 as the two galaxies with signs of AGN ionization.

galaxies. Since escape velocities derived via abundance matching are susceptible to significant systematic biases, we also estimated them using stellar velocities and dispersions. We determined the circular velocity, $v_{\rm circ} = \sqrt{(v_*^2 + \sigma_*^2)}$, where v_* and σ_* are the maximum stellar velocity and stellar dispersion, respectively. Note that this is a lower limit, as many of our rotation curves do not extend to the flat part of the curve. We then used the relation $v_{\rm esc} \approx 3v_{\rm circ}$ (Veilleux et al. 2020) to determine the escape velocity. We found that the escape velocities determined in this way are on average ∼30% higher than the escape velocities given in Table 4, indicating that an even lower fraction of the gas would be likely to escape.

5. Discussion

5.1. Comparison with AGN Dwarfs

There is a difference in kinematics, extent, and energetics between the SF dwarfs and AGN dwarfs. The average of the median values of v_{50} of the SF dwarfs, found in Section 4.1, is lower than the average of the median values of the AGN dwarfs (−64 km s^{-1}). Comparison of the maximally blueshifted velocities also shows that star-formation-driven outflows are slower than AGN-driven outflows (average of ∼−65 km s^{-1} for SF dwarfs versus −145 km s^{-1} for AGN dwarfs). The median values are redshifted or centered around 0, compared to the highly blueshifted values for AGN dwarfs. If we consider just the blueshifted v_{50} to contribute significantly to the outflow, we can see that there are very few blueshifted spaxels in the broad component of the SF dwarfs, whereas nearly all the spaxels in the broad component of the L20 AGN dwarfs are blueshifted. This could possibly indicate that strongly blueshifted outflows are not as prominent in SF dwarfs as they are in AGN dwarfs, and most of the effect of stellar activity may be to stir the gas rather than to expel it from the hosts.

The overall extent of stellar-driven outflows is greater than that of AGN-driven outflows as can be clearly seen in Figure 11. Note that the detectability limits were comparable in the measurement of outflow extent in both the SF and AGN samples. Therefore the difference in sizes is real and not a result of different sensitivities in the two samples. The AGN-driven outflows extend to distances between 0.3 and 3.1 kpc, with an average of 1.2 kpc. On the other hand, the stellar-powered outflows extend to further distances, between 1.2 and 3.2 kpc, with an average of 2.2 kpc. This could be because stellar-powered outflows may originate at multiple places within the galaxy (see Section 4.4), and are not necessarily confined to the center as AGN-powered outflows are. They can thus reach larger scales, even though they might not be as fast as AGN-powered outflows.

The mass, momentum, and kinetic energy rates are all much lower for the SF dwarfs than for the AGN dwarfs, as indicated in Figure 12. As mentioned earlier, assuming both the redshifted and blueshifted spaxels contribute to the outflows, we find that the values of the energetics increase by a small fraction, but overall they are still lower by 2 orders of magnitude compared to those of the AGN dwarfs.

The differences between the quantities in the two samples increase from the mass-loss rates to the momentum rates and are maximal for the energy rates. These calculations depend on both line luminosities and velocity terms. While the [O III] λ5007 luminosities of the AGN dwarfs are comparable to those of the SF dwarfs, the median v_{50} of the AGN-driven outflows are much higher than those of the SF-driven outflows.

The radial extent of the outflows could also play a role in lowering the energetics for the SF dwarfs, as the outflows are more radially extended than those of the AGN dwarfs.

The escape fractions from Table 4 for the SF galaxies are comparable to the escape fractions for the AGN galaxies. However, the AGN dwarfs have a maximum of 6% for two galaxies. Although these fractions are not significant enough to translate to an effective portion of the gas being ejected from the host galaxies by the outflows, they could still show that AGN dwarfs could play a more effective role in stirring up gas, which can considerably affect their environment. The escape velocities are also upper limits as they are calculated from the center of the galaxy, and we would also need to factor in the frequencies of these outflows.

5.2. Impact on the Galaxy

There is a significant difference between the outflows powered by AGNs and those powered by stellar processes. The lower speeds of the star-formation-driven outflows as compared to the AGN-driven outflows indicate that the gas is moving more slowly, and the lower energetic rates indicate that they are possibly not transporting large amounts of mass or energy from the galaxy. The greater values of kinematics and energetics from the AGN-driven outflows suggest that AGNs could play a more significant role in stripping the galaxy of gas and halting or slowing down star formation. Thus it is important to consider AGN contribution to feedback in dwarf galaxies in the study of galaxy evolution.

From the color–magnitude diagram for the AGN dwarfs and SF dwarfs presented in Figure 13, we see that the AGN dwarfs

are redder than the SF dwarfs. The correlation between galaxy colors and the nature of the galaxy has been extensively studied (Martin et al. 2007; Schawinski et al. 2007, 2010). The bluer colors of the SF dwarfs could indicate that their outflows have not played a significant role in effectively quenching star formation. On the other hand, the more energetic AGN-powered outflows may have hampered star formation. We note, however, that the positions of the galaxies in the color–magnitude diagram could be a selection effect, as it is generally easier to detect AGNs in galaxies with lower SFRs.

The extent of the SF outflows is found to be greater than that of the AGN outflows. This could indicate that the SF outflows can reach greater scales, and thus their overall time-averaged kinetic energy outflow rates appear lower. SF outflows could be comparable to AGN outflows in stirring up the gas at smaller scales in the host galaxy. The escape velocities could also be lower at these scales, so it would be easier for the material in the SF outflows to escape the host galaxy.

While star formation could be instantaneously less energetic compared to AGN-driven outflows, it is important to consider the long-term effects of the two processes. Multiple bursts from stellar activity could lead to stellar processes dominating over AGN-driven outflows in regulating the environment of the galaxy. For AGN-driven outflows to be significant over a long time, it would be important to consider the duty cycles of AGN activity or how frequently AGN-powered outflows occur as compared to stellar-driven outflows.

5.3. Comparison with Previous Studies

A number of studies have measured the kinematics of ionized gas in dwarf galaxies, and we compare our results with some of the work found in the literature. Schwartz & Martin (2004) used high-resolution echelle spectrographs to study the Na D absorption lines in six nearby dwarf starburst galaxies. They discovered that three of them have outflows, with an average outflow velocity of -27 km s^{-1}. This is lower (more blueshifted) than our median v_{50} values. However, our maximum blueshifted v_{50} values for the broad component are comparable.

van Eymeren et al. (2009) looked at emission lines in H I and Hα to estimate outflow velocities in the nearby SF irregular dwarf galaxy NGC 2366. They characterized the galaxy as having two major outflows, one with blueshifted velocities of 30 km s^{-1} and the other with redshifted velocities up to 50 km s^{-1} with a radial extent of 1.4 kpc. It is interesting that they considered redshifted velocities to indicate an outflowing component, in contrast to our analysis. We find that if we consider the redshifted velocities in our calculations of the energetics, the values do not change significantly. However, it would imply that it is possible that the redshifted velocities in our C2 maps are indicative of actual outflowing gas.

Our results are also in line with Marasco et al. (2023), who studied ionized gas kinematics in a sample of 19 nearby starburst galaxies. The line profile they observed as depicted in their Figure 6 also appears to be symmetric, and there is no apparent blueshift. They found ionized gas outflow rates in the range of 10^{-4}–10^{-1} $M_{\odot}$ yr^{-1}, which is an order of magnitude higher than the values calculated in this work for SF dwarfs. However, they still concluded that stellar feedback only stimulates a gentle gas cycle and is less likely to cause major blowouts that affect the evolution of the dwarf galaxy.

Manzano-King et al. (2019) observed 3 of the 10 SF dwarfs in this work and found wind speeds that are much higher than what we measured. This could be due to the fact that they defined outflow velocity differently from this work. It could also be attributed to the slit spectroscopy used as compared with the higher resolution power of KCWI and the larger field of view, which helped us make more accurate measurements. Some differences in profiles were also observed by L20 in their comparison of KCWI data with LRIS data for the AGN dwarfs. While the results generally agreed, they found that for two of the targets, the KCWI data showed narrower profiles with smaller blueshifts as compared to the LRIS data (for a more in-depth analysis, refer to Section 4.3 in L20).

Our analysis shows that stellar feedback might be less significant than previously expected. With the spatial information provided by IFS, we are able to see the effects of stellar-powered outflows in galaxies. There appear to be some regions of strong outflow activity, but even then, it is not as powerful as AGN activity. It is possible that, at least in many cases, stellar feedback might only disturb the gas locally and not have major effects on the host galaxy as a whole.

6. Summary and Conclusions

In this paper, we report the results from a Keck/KCWI integral field spectroscopic study of a sample of 10 low-redshift SF dwarf galaxies with ionized gas outflows. This study is a companion study to L20, so we also compare our results to those for their sample of dwarf galaxies with AGN-powered outflows.

1. The [O III] λ5007 emission line shows a clear broad component in all our targets, indicating either outflowing or disturbed gas in the galaxy. These broad components have more symmetric line profiles and are less blueshifted than those found in the sample of AGN dwarfs, with an average v_{50} close to 0 km s^{-1}, and an average value of W_{80} of 484 km s^{-1} across the 10 targets. In contrast, the broad component of the [O III] λ5007 lines in the AGN dwarfs shows strong blueshifts with an average $v_{50} \sim -64$ km s^{-1}. Nevertheless, the average values of W_{80} in both samples are comparable ($\sim$456 km s^{-1} for the AGN dwarfs).
2. All of the outflows detected in the SF dwarfs are spatially resolved with sizes up to two to three times the half-light radius of the galaxies. These outflows are significantly more extended than those of the AGN dwarfs. While the latter show a biconical structure in some cases, the stellar-driven outflows tend to be more spherically symmetric.
3. We calculate the ionized mass in the outflows, and the mass-loss rates (*dM/dt*), kinetic energy rates (*dE/dt*), and momentum rates (*cdp/dt*). These energetics help us determine how much of the gas mass is being carried out by the outflows and, in turn, can let us know how potentially effective the outflows can be in influencing the evolution of the galaxy. We find that the values of ionized gas mass in the outflows range from $\sim 3 \times 10^{-5}$ to 2×10^{-2} $M_{\odot}$ yr^{-1}, and the kinetic energy rates for the outflows range from $\sim 2 \times 10^{35}$ to 1×10^{38} erg s^{-1}. These values for the SF outflows are all lower than the corresponding values for the AGN-driven outflows, with

the energy outflow values being 2–3 orders of magnitude lower.

4. A small fraction (<2%) of the outflowing ionized gas in the targets has velocities higher than the escape velocities of the host galaxy, calculated from the center of the galaxy. These values are similar to the ones found by L20 for the AGN-driven outflows.

Thus we find that SF dwarfs clearly have significantly lower values of energetics in the outflows as compared to AGN dwarfs. This is despite the fact that our sample of SF dwarfs is biased toward stronger outflows, since we have selected the targets that show the clearest and broadest second components to the [O III] λ5007 emission lines. Determining the relative importance between AGN feedback and SF feedback in the evolution of dwarf galaxies will require detailed models that take into consideration factors such as duty cycles and black hole occupation fractions, as well as the energetics presented in this study and those of L20. What is certainly clear is that AGN feedback is an important ingredient that cannot be ignored in the study of dwarf galaxy evolution.

Acknowledgments

We thank the anonymous referee for thoughtful feedback and constructive comments that greatly helped to improve this paper. The authors would also like to thank Laura Sales for her useful comments on the paper and Marie Wingyee Lau for her support with IFSFIT. Partial support for this project was provided by the National Science Foundation under grant No. AST 1817233. V.U. acknowledges funding support from NASA Astrophysics Data Analysis Program (ADAP) grant 80NSSC20K0450. The data presented herein were obtained at the W. M. Keck Observatory, which is operated as a scientific partnership among the California Institute of Technology, the University of California, and the National Aeronautics and Space Administration. The observatory was made possible by the generous financial support of the W. M. Keck Foundation. The authors wish to recognize and acknowledge the very significant cultural role and reverence that the summit of Maunakea has always had within the indigenous Hawaiian community. We are most fortunate to have the opportunity to conduct observations from this mountain.

Facilities: Sloan, Keck:II (KCWI).

Software: astropy (Astropy Collaboration et al. 2013, 2018), BADASS (Sexton et al. 2020), IFSFIT (Rupke 2014b), IFSRED (Rupke 2014a), MPFIT (Markwardt 2012), pPXF (Cappellari 2017), SciencePlots (Garrett 2021), Source Extractor (Bertin & Arnouts 1996).

Appendix A
[O III] λ5007 Flux, Velocity, and Stellar Kinematic Maps

The detailed results from our analysis are presented in this appendix. We show the [O III] λ5007 flux maps, the v_{50} maps, and the W_{80} velocity maps for the narrow velocity component (C1), the broad velocity component (C2), and the total. We also show the radial profile of each target in Appendix B. In all cases, the systemic velocities were determined from the stellar velocities measured from the stellar absorption lines in the spectra integrated over the whole cube.

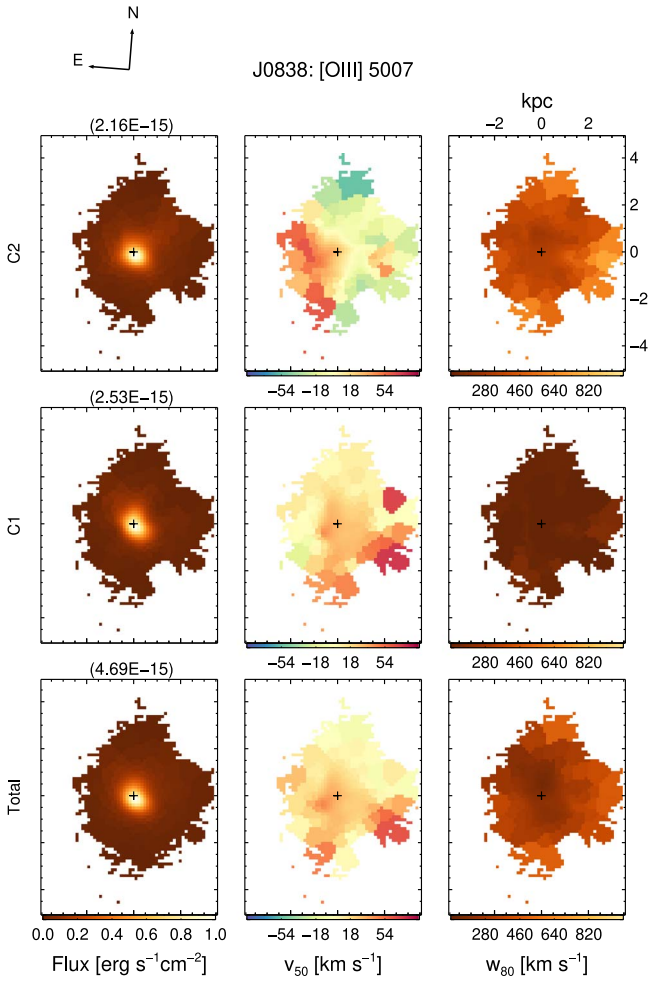

Figure 14. Voronoi-binned [O III] λ5007 flux maps for J0838 in the leftmost panel, v_{50} maps in the middle panel, and W_{80} velocity maps in the rightmost panel. The first row is for C2, the second row is for C1, and the third row (Total) represents the overall emission profile. The maximum value of the flux in cgs units is indicated above the flux maps in the leftmost panels. The axis represents the extent in kiloparsecs and the orientation of the maps is indicated by the black compass on the top left of the figure.

A.1. J0838

Figure 14 shows maps of the [O III] λ5007 flux, velocity, and stellar kinematics for J0838. The first row represents the broad component, the second row represents the narrow component, and the third row of panels represents the total flux map. The flux is normalized to the value indicated by the black cross to mark the approximate center of the galaxy. This is slightly different from the case of L20, who marked the black cross with the highest flux value, which also coincided with the center of the galaxy due to the nature of AGN dwarfs. In our sample, the maximum value of the flux need not be close to the center as there is no preferential location for strong stellar activity. To maintain uniformity with the L20 analysis, we consider our normalizing flux value to come from a spaxel in the apparent center of the galaxy. The maximum values of the flux are indicated above the panels. The plot of the C2 flux shows some extended emissions distinct from those traced by C1.

The C2 v_{50} values have a significant gradient compared to the C1 values. There does not seem to be a strongly blueshifted

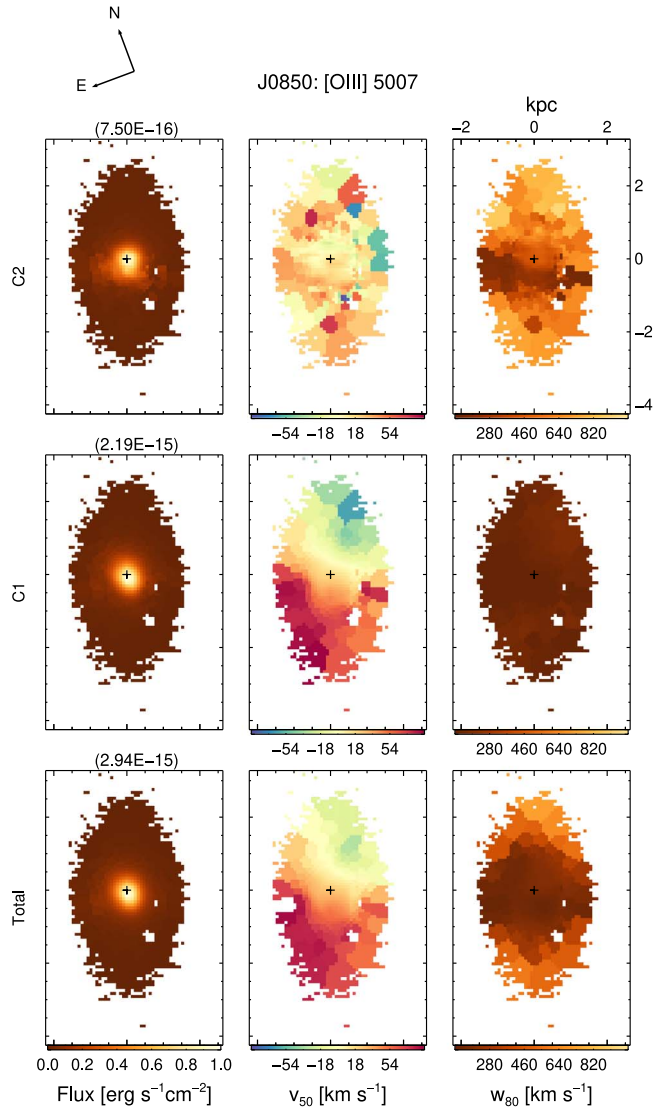

Figure 15. Same as Figure 14, but for J0850.

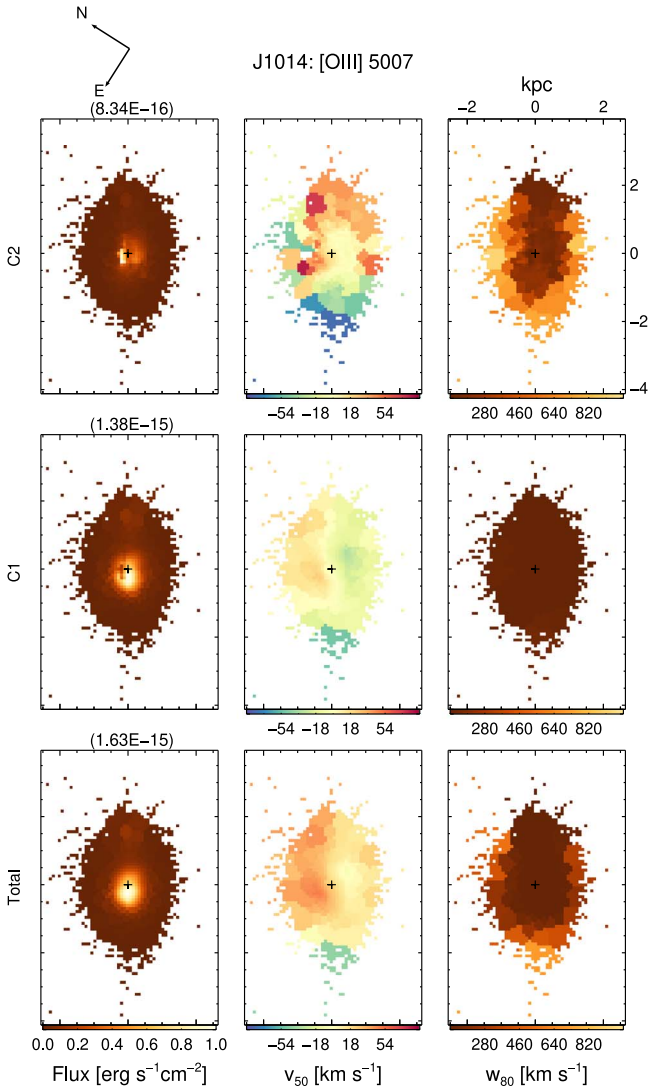

Figure 16. Same as Figure 14, but for J1014.

component, but there is evidence of a redshifted component. In contrast, the C1 velocities are relatively quiescent with some being very close to 0 km s^{-1}. The strongly redshifted blobs on the right are likely due to noise and do not have any physical meaning. The v_{50} maps of the broad component are clearly distinct from those of the narrow component, indicating that the broad component does not trace the gas in the galaxy. There are also no apparent correlations between the C2 flux and the strength of the velocity maps.

The relation between W_{80} and σ indicating dispersion in the line profile is given as $W_{80} = 2.63\sigma$. The W_{80} maps indicate that the narrow component does not have a wide dispersion, which is expected as the narrow component traces the quiescent gas in the galaxy. In contrast, the broad component clearly has greater values of W_{80}, showing that the component it traces is significantly disturbed. These values range between 300 and 700 km s^{-1}, with a median of 397 km s^{-1}.

A.2. J0850

In the [O III] λ5007 flux maps for J0850 indicated in Figure 15, the C2 flux component shows an extended flux making it distinct from the C1 flux component. The velocity maps of C1 show that the systemic gas in the galaxy is likely rotating. However, we see that the C2 component once again does not trace the gas in the galaxy. There does not seem to be a pattern in the C2 velocity maps, but that could just indicate that the broad component is tracing stirred and disturbed gas in the galaxy, which could be caused by stellar processes. The average value of the C2 v_{50} is roughly 0 km s^{-1} when computed over the entire galaxy. The W_{80} maps for C2 seem to trace certain regions of low dispersion, and other regions show higher dispersion, which could possibly indicate turbulence caused by the C2 component.

A.3. J1014

Figure 16 traces the [O III] λ5007 flux and velocity maps. The C2 flux component seems diminished, indicating that there is not much contribution from the broad component to the flux. There seems to be a faint blob near the top, but it is more prominent in the C1 flux map as compared to C2. It also does not translate over to the v_{50} maps, as we do not see any corresponding distinct feature near the top of these maps. The

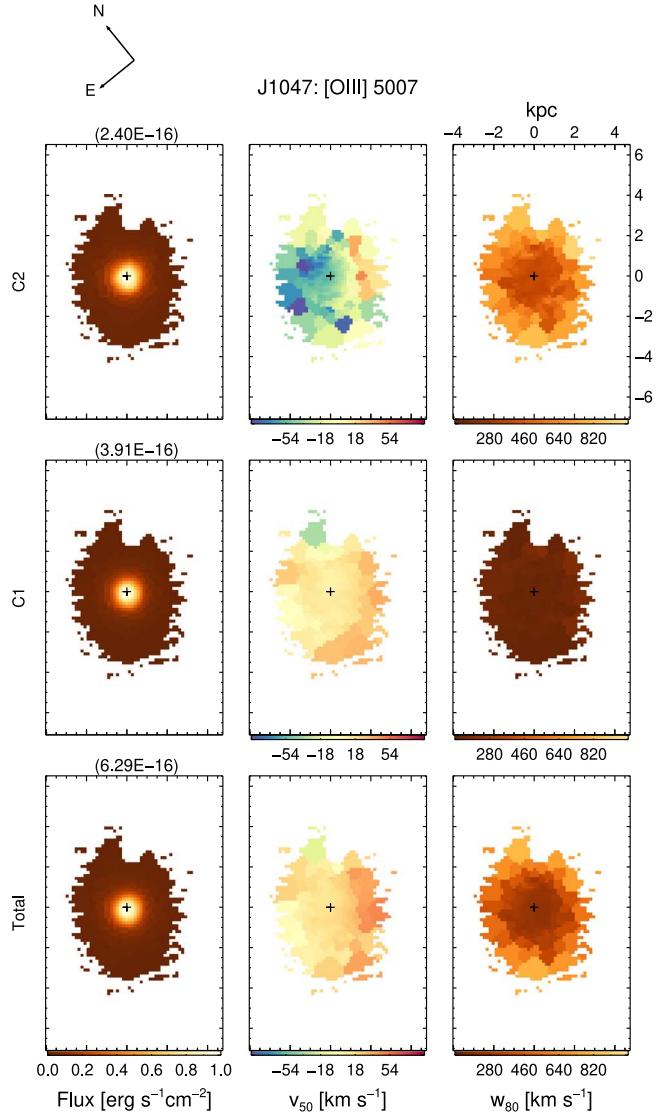

Figure 17. Same as Figure 14, but for J1047.

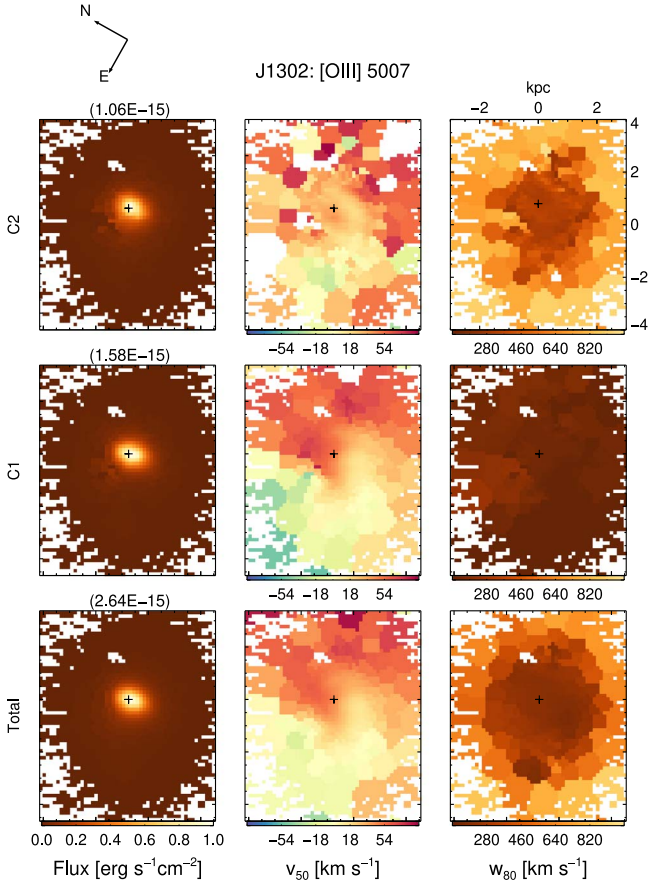

Figure 18. Same as Figure 14, but for J1302.

C1 component v_{50} appears quiescent, and the bottom blue component is out of place and is likely caused by noise. The C2 v_{50} does not have any significant features, although it does appear to be more strongly redshifted as compared to the narrow gas component. The velocity dispersion indicated by the W_{80} maps is also higher in the outer regions for C2, and there seems to be a region of lower dispersion being traced out as well.

A.4. J1047

From Figure 17, we see that the v_{50} maps for C2 are clearly distinct from those for C1. They appear to be more blueshifted, indicating that this target likely has some prominent stellar outflows, also indicated by the high values of dispersion from the W_{80} velocity maps for C2. C1 is once again quiescent with little dispersion.

A.5. J1302

Figure 18 shows the [O III] λ5007 flux maps and velocity maps for J1302. C1 traces the gas in the galaxy and shows that it is likely to be rotating. The C2 velocity maps do not follow the rotation but they do not have any distinct features. They mostly seem to have low velocity values, although they do show significant dispersion in their W_{80} values as compared to C1.

A.6. J1307

From Figure 19, it is evident that J1307 has multiple sources (visible in the flux maps). They appear to be fainter in the C2 maps as compared to the C1 maps, suggesting that these sources likely do not contribute to the broad component. The v_{50} maps of C1 show some rotation in the galaxy, but there does not seem to be a strong correlation between the bright-flux region in the flux map and the velocity maps. There are slightly blueshifted velocities observable in the C2 velocity map in the regions around the bright sources, but they are not significantly high. It is possible that the bright-flux region corresponds to another stellar source producing high ionization activity, but it still does not produce fast outflows. This is supported by the absence of significant dispersion in the W_{80} velocity maps in the same region.

A.7. J1325

The C2 v_{50} map (Figure 20) shows that the outflow is either rotating or oriented biconically. In either case, it is clearly distinct from the C1 gas component, which is nearly quiescent. This indicates that the gas in the galaxy is nearly stationary, but there is a distinct outflow present. The C2 W_{80} velocity map

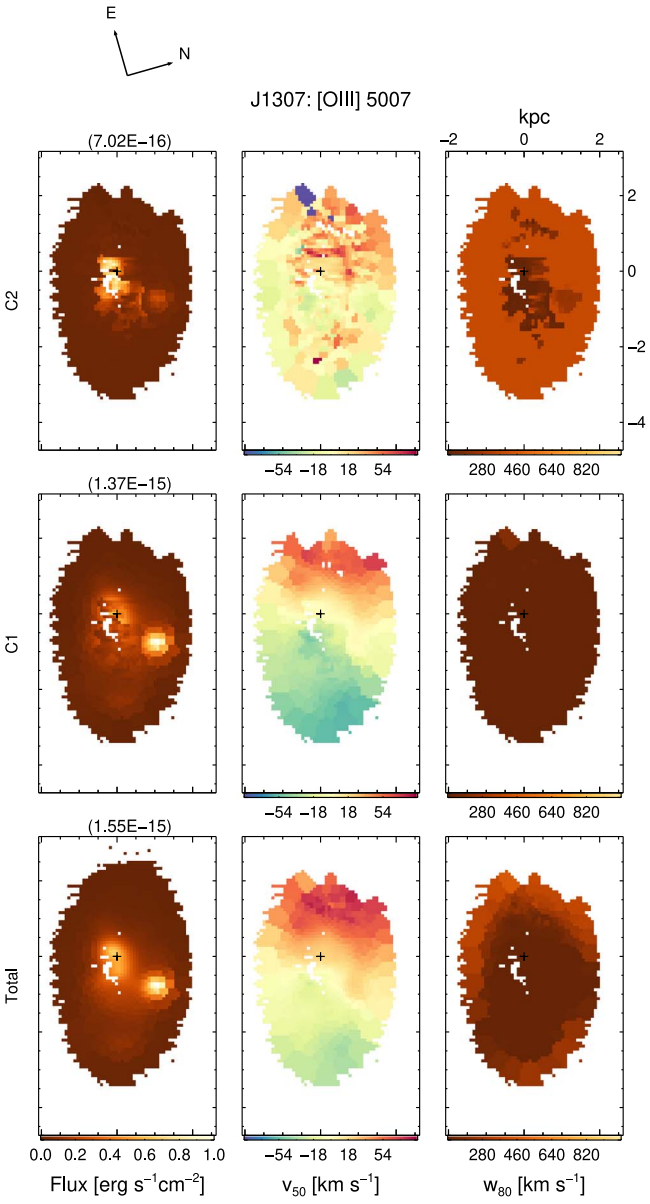

Figure 19. Same as Figure 14, but for J1307.

also shows a significant dispersion, unlike the C1 W_{80} velocity map.

A.8. J1415

The C2 v_{50} map (Figure 21) shows some regions of blueshift, which could indicate an outflow. It is distinct once again from the C1 v_{50} map, which is mostly quiescent but has some hints of a rotating gas. The C2 W_{80} velocity map also shows significant dispersion indicating that C2 is distinct from the C1 quiescent gas.

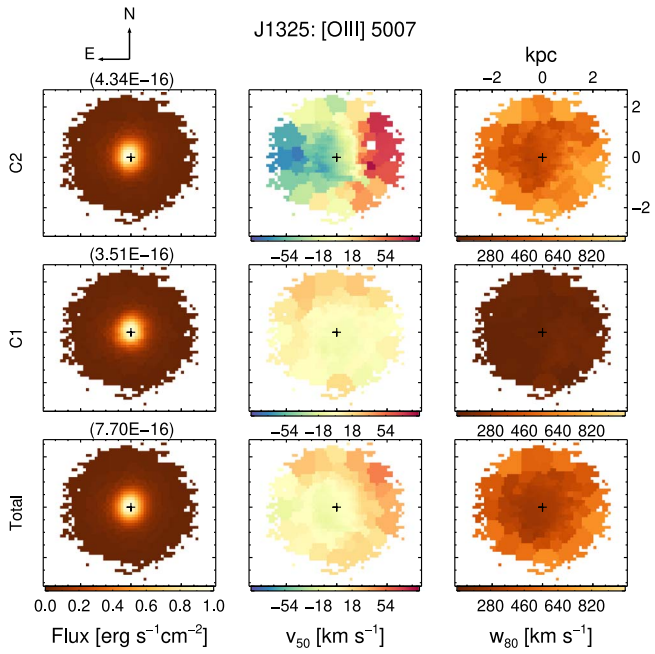

Figure 20. Same as Figure 14, but for J1325.

A.9. J1622

The v_{50} flux maps of J1622 (Figure 22) show extremely interesting structures going from C1 to C2. The C2 component can constitute an outflow because of the significant blueshift in the velocities but they appear to be oriented perpendicularly to the rotating gas in the galaxy. The significant velocity dispersion in the C2 W_{80} velocity map is indicative of an outflow. The narrow component does not have a significant dispersion once again.

A.10. J1717

J1717 is at the lowest redshift compared to the rest of the galaxies and thus occupies a larger fraction in the sky. The galaxy appears extended and also has interesting flux maps as seen in Figure 23. The C1 flux map indicates the presence of several sources of SF regions near the center and one slightly near the bottom, which is only faintly seen in the C2 flux map. The galaxy also appears to have a rotating gas component as seen in the C1 v_{50} map. The C2 component seems to trace this gas slightly based on the rotating pattern observed, but it has lower values of v_{50}. There also does not seem to be a prominent dispersion, although the map is significantly noisy. We could not go to higher S/N as we started losing spatial information. There seems to be a slight visual correlation between the flux maps and the velocity maps near the regions of the additional sources, although it is not too apparent from the W_{80} velocity maps. This is different from the case of J1307, for which we also have obvious multiple sources but no apparent correlations between the flux and velocity maps (see Figure 19).

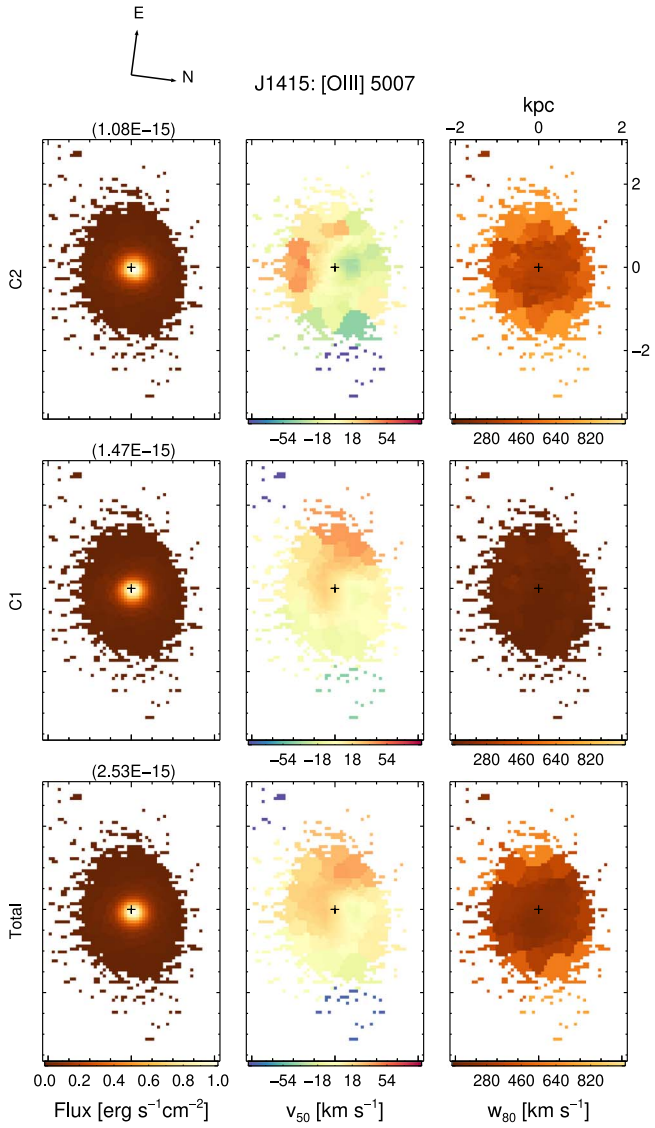

Figure 21. Same as Figure 14, but for J1415.

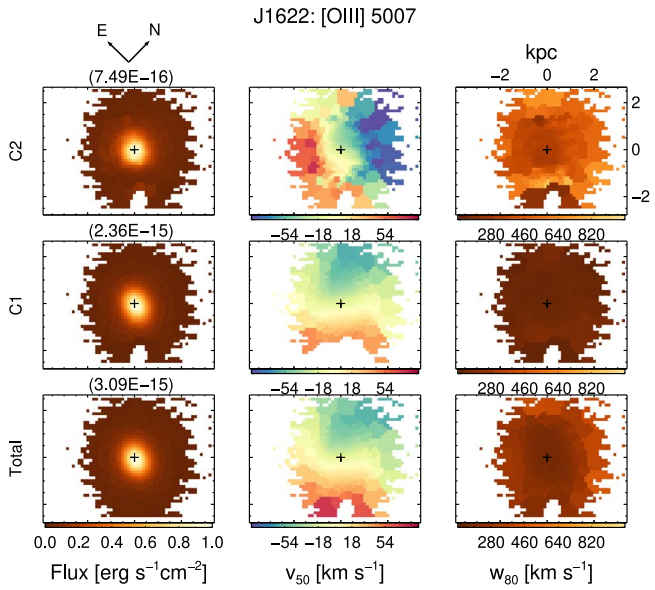

Figure 22. Same as Figure 14, but for J1622.

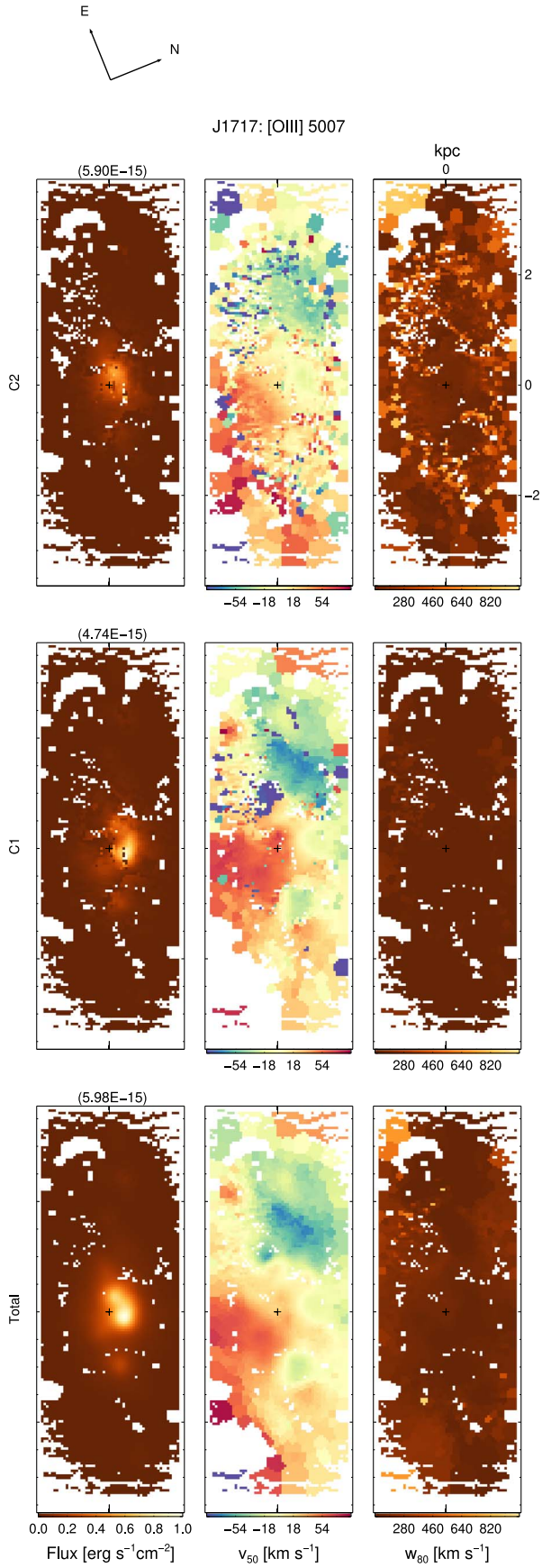

Figure 23. Same as Figure 14, but for J1717.

Appendix B
Radial Flux Profiles

The radial flux profiles of the targets are plotted in Figures 24 and 25. The black solid line is the PSF of a standard star observed close to the target to reduce errors due to the atmosphere. We then plot the individual velocity components and see that they are spatially resolved in the KCWI data. The bottom plot shows that the ratio of C2 flux to C1 flux increases at greater distances, showing that the two components have different flux distributions.

The radial flux profiles of J0850 are plotted in Figure 25(a). The panels and plots are the same as those mentioned in Figure 24. There seem to be two distinct streams being traced out by the C2 component, which are seen in both panels. This could be due to the thin band spotted in the middle of the C2 flux maps in Figure 15, which indicates that there are two different flux values at the same distance on either side of the central spaxel used for the flux normalization. It is clearly distinct from the C1 component that traces the quiescent gas.

The radial flux profiles of J1307 are plotted in Figure 25(e). The lower values of the normalized flux near the center indicate that the flux in the broad component peaks at a distance further away from the center of the galaxy. The presence of multiple sources is evident from the peaks present in the profile, which can be seen in both the components; this indicates that the broad component may also trace the multiple sources, which is not very evident in the flux and velocity maps in Figure 19. The radial profile is still spatially extended.

The radial flux profile of J1717 in Figure 25(i) is crowded due to a large number of pixels. However, the spatially extended profile is visible and there are also multiple peaks that can be discerned in the profile. The C2 component also seems to trace the peaks, which could indicate that additional sources could contribute to the broad component.

For the rest of the targets, the [O III] λ5007 flux radial profile is clearly more extended than the PSF, which is consistent with the spatially resolved velocity gradients seen in both the ionized gas and the underlying stellar population.

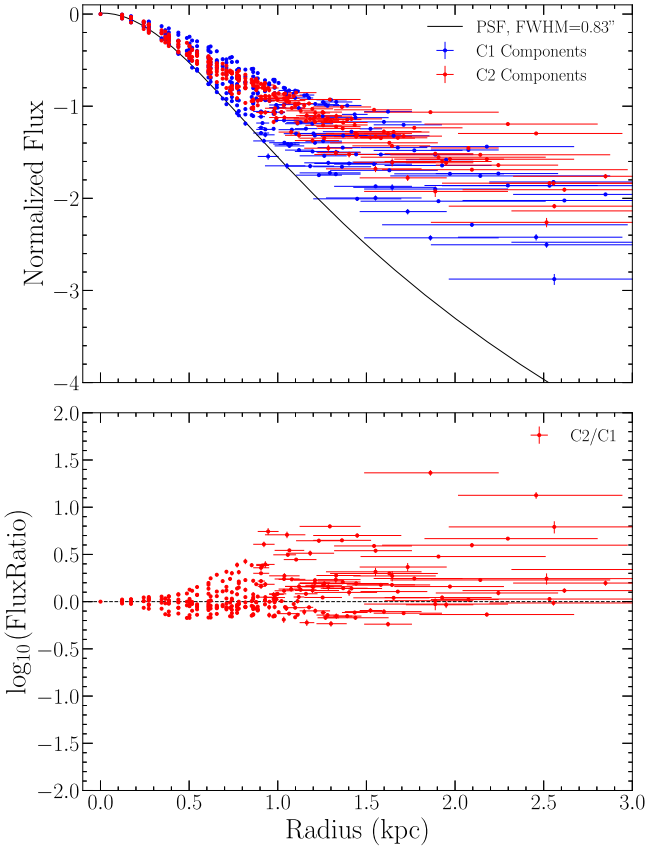

Figure 24. Top panel: The radial profiles of [O III] λ5007 fluxes for the two velocity components of J0838. Here, the fluxes are normalized to their maximum value. The PSF profile is obtained by fitting a Moffat profile to the spectrophotometric standard star (see Section 2.2 for more details). Bottom panel: C2/C1 flux ratios plotted on a logarithmic scale as a function of distance from the spaxel marked by the black cross in Figure 14. The error bars on the x-axis indicate the radial coverage of the spatial bin.

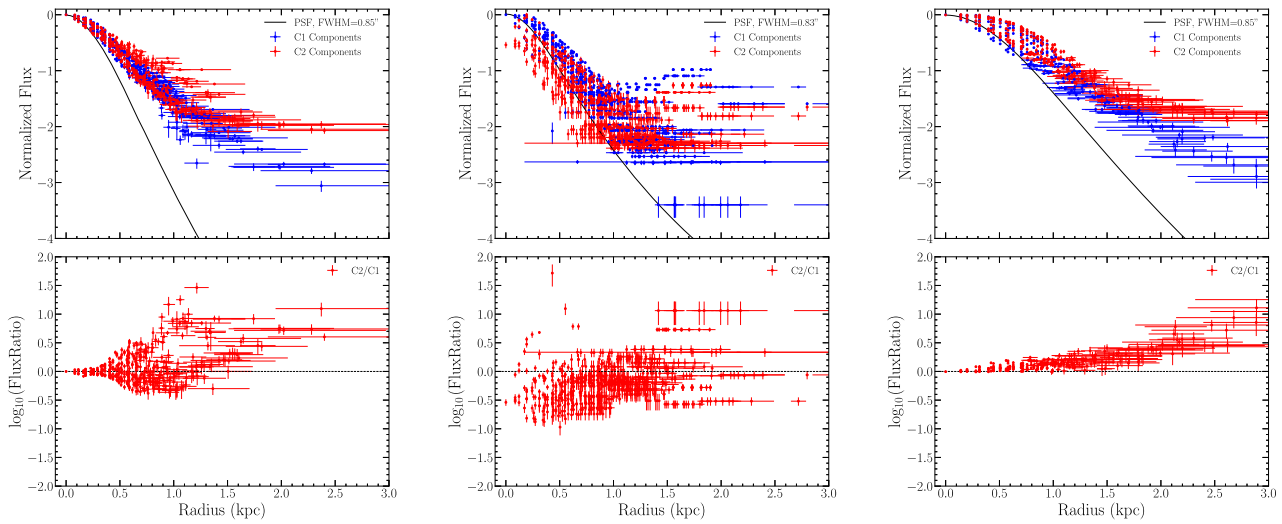

(a) J0850

(b) J1014

(c) J1047

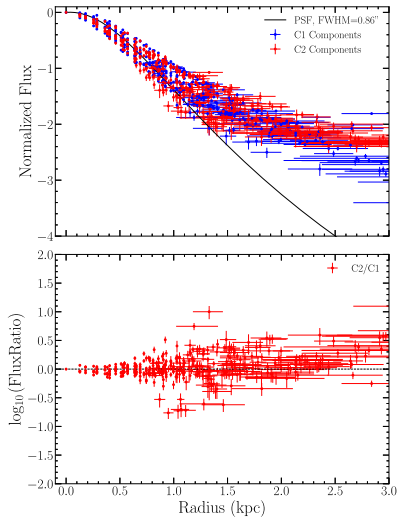

(d) J1302

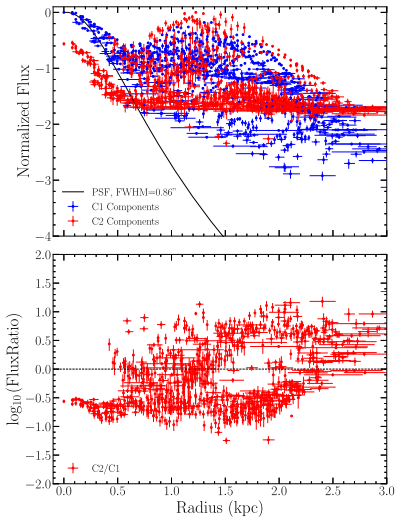

(e) J1307

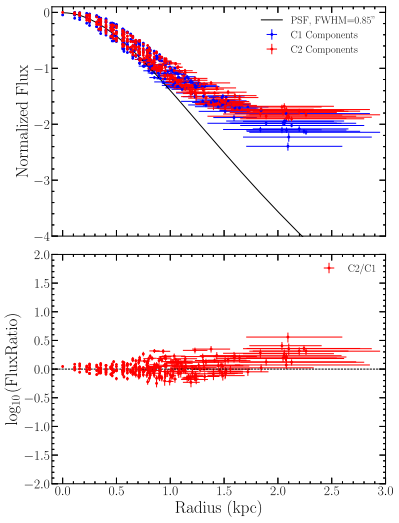

(f) J1325

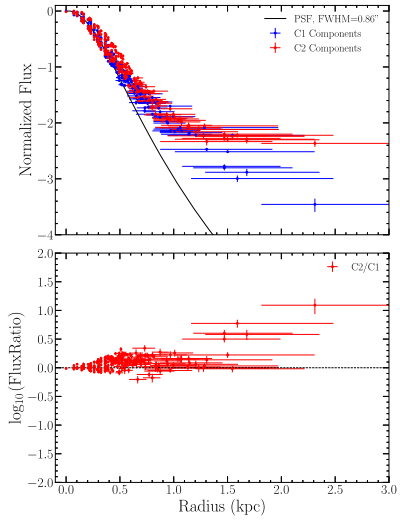

(g) J1415

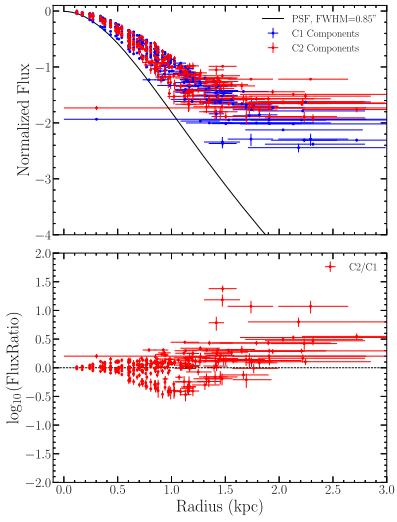

(h) J1622

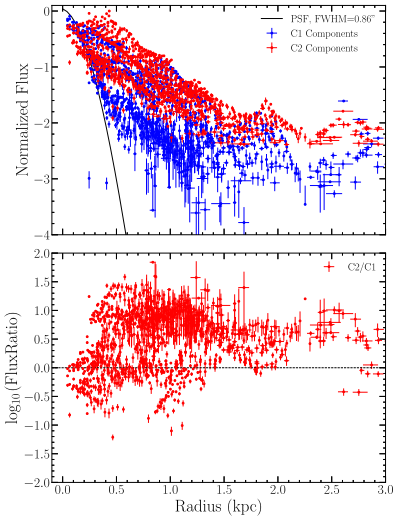

(i) J1717

Figure 25. Same as Figure 24, but for the rest of the targets.

ORCID iDs

Archana Aravindan https://orcid.org/0000-0001-7578-2412
Weizhe Liu https://orcid.org/0000-0003-3762-7344
Gabriela Canalizo https://orcid.org/0000-0003-4693-6157
Sylvain Veilleux https://orcid.org/0000-0002-3158-6820
Thomas Bohn https://orcid.org/0000-0002-4375-254X
Remington O. Sexton https://orcid.org/0000-0003-3432-2094
David S. N. Rupke https://orcid.org/0000-0002-1608-7564
Vivian U https://orcid.org/0000-0002-1912-0024

References

Astropy Collaboration, Price-Whelan, A. M., Sipőcz, B. M., et al. 2018, AJ, 156, 123
Astropy Collaboration, Robitaille, T. P., Tollerud, E. J., et al. 2013, A&A, 558, A33
Baldwin, J. A., Phillips, M. M., & Terlevich, R. 1981, PASP, 93, 5
Bertin, E., & Arnouts, S. 1996, A&AS, 117, 393
Boylan-Kolchin, M., Bullock, J. S., & Kaplinghat, M. 2011, MNRAS, 415, L40
Boylan-Kolchin, M., Bullock, J. S., & Kaplinghat, M. 2012, MNRAS, 422, 1203
Brinchmann, J., Charlot, S., White, S. D. M., et al. 2004, MNRAS, 351, 1151
Cappellari, M. 2017, MNRAS, 466, 798
Cappellari, M., & Copin, Y. 2003, MNRAS, 342, 345
Cappellari, M., & Emsellem, E. 2004, PASP, 116, 138
Cardelli, J. A., Clayton, G. C., & Mathis, J. S. 1989, ApJ, 345, 245
Chambers, K. C., Magnier, E. A., Metcalfe, N., et al. 2016, arXiv:1612.05560
Concas, A., Popesso, P., Brusa, M., et al. 2017, A&A, 606, A36
Dashyan, G., Silk, J., Mamon, G. A., Dubois, Y., & Hartwig, T. 2018, MNRAS, 473, 5698
Davies, R. L., Förster Schreiber, N. M., Übler, H., et al. 2019, ApJ, 873, 122
Dubinski, J., & Carlberg, R. G. 1991, ApJ, 378, 496
Garrett, J. D. 2021, garrettj403/SciencePlots v2.1.0, Zenodo, doi:10.5281/zenodo.4106649
Garrison-Kimmel, S., Rocha, M., Boylan-Kolchin, M., Bullock, J. S., & Lally, J. 2013, MNRAS, 433, 3539
González Delgado, R. M., Cervi no, M., Martins, L. P., Leitherer, C., & Hauschildt, P. H. 2005, MNRAS, 357, 945
Greene, J. E., & Ho, L. C. 2007, ApJ, 670, 92
Harrison, C. M., Alexander, D. M., Mullaney, J. R., & Swinbank, A. M. 2014, MNRAS, 441, 3306
Heckman, T. M., Miley, G. K., van Breugel, W. J. M., & Butcher, H. R. 1981, ApJ, 247, 403
Hinshaw, G., Larson, D., Komatsu, E., et al. 2013, ApJS, 208, 19
Kauffmann, G., Heckman, T. M., White, S. D. M., et al. 2003, MNRAS, 341, 33
Kewley, L. J., Dopita, M. A., Sutherland, R. S., Heisler, C. A., & Trevena, J. 2001, ApJ, 556, 121
Kewley, L. J., Geller, M. J., & Jansen, R. A. 2003, AAS Meeting, 203, 119.01
Kewley, L. J., Geller, M. J., & Jansen, R. A. 2004, AJ, 127, 2002
Klypin, A., Kravtsov, A. V., Valenzuela, O., & Prada, F. 1999, ApJ, 522, 82
Koudmani, S., Henden, N. A., & Sijacki, D. 2021, MNRAS, 503, 3568
Koudmani, S., Sijacki, D., & Smith, M. C. 2022, MNRAS, 516, 2112
Larson, R. B. 1974, MNRAS, 169, 229
Lau, M. W., Prochaska, J. X., & Hennawi, J. F. 2018, ApJ, 857, 126
Li, B.-S., Li, G.-L., Cheng, J., Peterson, J., & Cui, W. 2016, RAA, 16, 139
Liu, W., Veilleux, S., Canalizo, G., et al. 2020, ApJ, 905, 166
Manzano-King, C. M., Canalizo, G., & Sales, L. V. 2019, ApJ, 884, 54
Marasco, A., Belfiore, F., Cresci, G., et al. 2023, A&A, 670, A92
Markwardt, C. 2012, MPFIT: Robust nonlinear least squares curve fitting, Astrophysics Source Code Library, ascl:1208.019
Martin, D. C., Wyder, T. K., Schiminovich, D., et al. 2007, ApJS, 173, 342
Martín-Navarro, I., & Mezcua, M. 2018, ApJL, 855, L20
Mashchenko, S., Wadsley, J., & Couchman, H. M. P. 2008, Sci, 319, 174
Matzko, W., Satyapal, S., Ellison, S. L., et al. 2022, MNRAS, 514, 4828
Mezcua, M., & Domínguez Sánchez, H. 2020, ApJL, 898, L30
Moffat, A. F. J. 1969, A&A, 3, 455
Molina, M., Reines, A. E., Latimer, L. J., Baldassare, V., & Salehirad, S. 2021, ApJ, 922, 155
Moore, B., Ghigna, S., Governato, F., et al. 1999, ApJL, 524, L19
Moran, E. C., Shahinyan, K., Sugarman, H. R., Vélez, D. O., & Eracleous, M. 2014, AJ, 148, 136
Morrissey, P., Matuszewski, M., Martin, D. C., et al. 2018, ApJ, 864, 93
Moster, B. P., Naab, T., & White, S. D. M. 2013, MNRAS, 428, 3121
Navarro, J. F., Frenk, C. S., & White, S. D. M. 1996, ApJ, 462, 563
Ogiya, G., & Mori, M. 2011, ApJL, 736, L2
Osterbrock, D. E., & Ferland, G. J. 2006, Astrophysics of Gaseous Nebulae and Active Galactic Nuclei (Mill Valley, CA: Univ. Science Books)
Penny, S. J., Masters, K. L., Smethurst, R., et al. 2018, MNRAS, 476, 979
Ramos Almeida, C., Acosta-Pulido, J. A., Tadhunter, C. N., et al. 2019, MNRAS, 487, L18
Reines, A. E., Greene, J. E., & Geha, M. 2013, ApJ, 775, 116
Rupke, D. S. N. 2014a, IFSRED: Data Reduction for Integral Field Spectrographs, Astrophysics Source Code Library, ascl:1409.004
Rupke, D. S. N. 2014b, IFSFIT: Spectral Fitting for Integral Field Spectrographs, Astrophysics Source Code Library, ascl:1409.005
Rupke, D. S. N., & Veilleux, S. 2013a, ApJL, 775, L15
Rupke, D. S. N., & Veilleux, S. 2013b, ApJ, 768, 75
Rupke, D. S. N., & Veilleux, S. X. 2015, ApJ, 801, 126
Sales, L. V., Wetzel, A., & Fattahi, A. 2022, NatAs, 6, 897
Sanders, R. L., Shapley, A. E., Kriek, M., et al. 2016, ApJ, 816, 23
Sawala, T., Frenk, C. S., Fattahi, A., et al. 2016, MNRAS, 457, 1931
Schawinski, K., Thomas, D., Sarzi, M., et al. 2007, MNRAS, 382, 1415
Schawinski, K., Urry, C. M., Simmons, B. D., et al. 2014, MNRAS, 440, 889
Schawinski, K., Urry, C. M., Virani, S., et al. 2010, ApJ, 711, 284
Schlegel, D. J., Finkbeiner, D. P., & Davis, M. 1998, ApJ, 500, 525
Schwartz, C. M., & Martin, C. L. 2004, ApJ, 610, 201
Sexton, R. O., Matzko, W., Darden, N., Canalizo, G., & Gorjian, V. 2020, MNRAS, 500, 2871
Shih, H.-Y., & Rupke, D. S. N. 2010, ApJ, 724, 1430
Sijacki, D., Vogelsberger, M., Genel, S., et al. 2015, MNRAS, 452, 575
van Eymeren, J., Koribalski, B. S., López-Sánchez, A. ´R., Dettmar, R. J., & Bomans, D. J. 2010, MNRAS, 407, 113
van Eymeren, J., Marcelin, M., Koribalski, B., et al. 2009, A&A, 493, 511
Veilleux, S., Cecil, G., & Bland-Hawthorn, J. 2005, ARA&A, 43, 769
Veilleux, S., Maiolino, R., Bolatto, A. D., & Aalto, S. 2020, A&ARv, 28, 2
Veilleux, S., & Osterbrock, D. E. 1987, ApJS, 63, 295
Veilleux, S., Teng, S. H., Rupke, D. S. N., Maiolino, R., & Sturm, E. 2014, ApJ, 790, 116